SANDIA REPORT
SAND2018-9380
Unlimited Release
Printed August, 2018

Dispersion Validation for Flow Involving a Large Structure

Alexander L. Brown, Erik Benavidez

Prepared by
Sandia National Laboratories
Albuquerque, New Mexico 87185 and Livermore, California 94550

Sandia National Laboratories is a multimission laboratory managed and operated by National Technology and Engineering Solutions of Sandia, LLC., a wholly owned subsidiary of Honeywell International, Inc., for the U.S. Department of Energy's National Nuclear Security Administration under contract DE-NA-0003525.

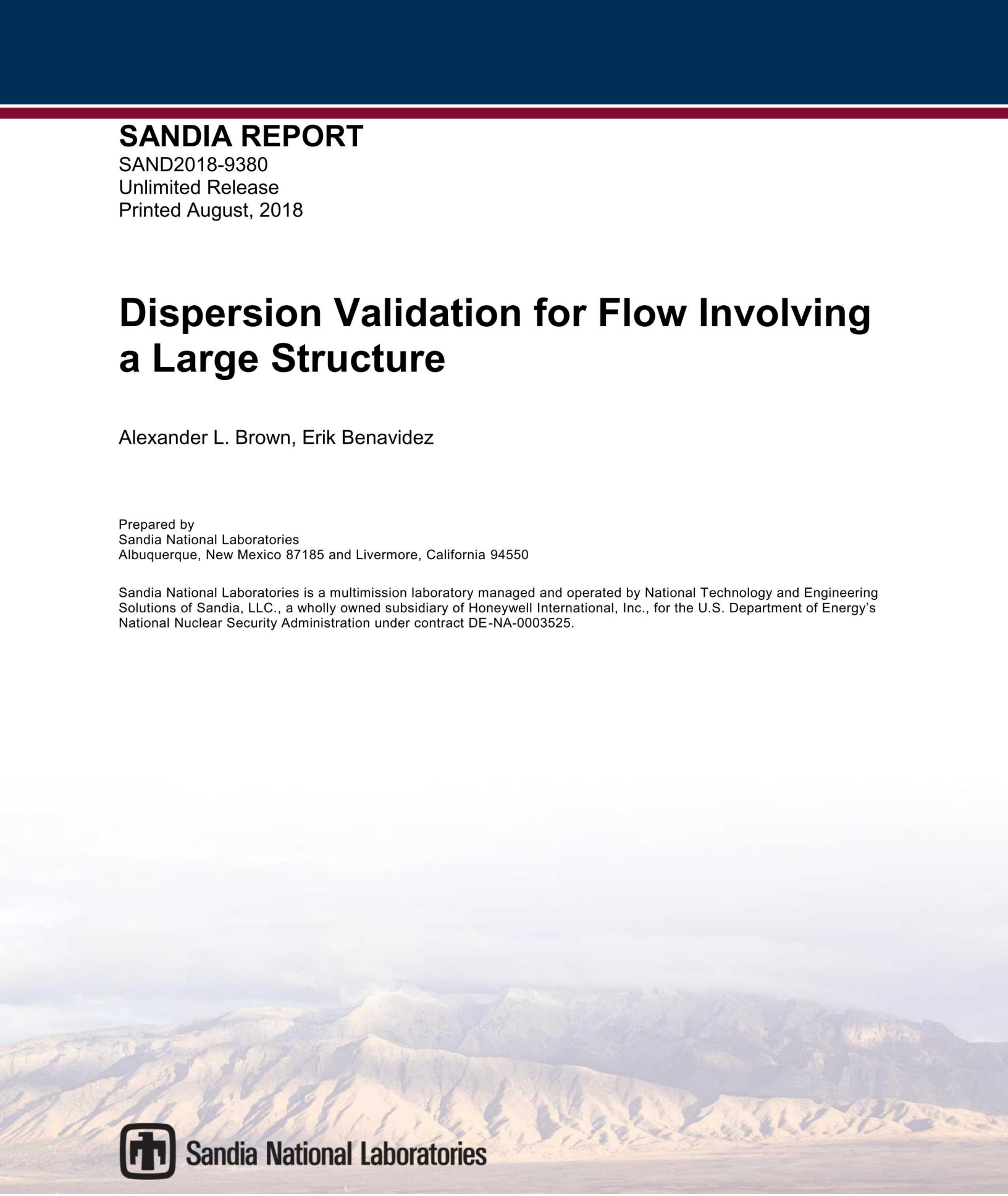

Issued by Sandia National Laboratories, operated for the United States Department of Energy by National Technology and Engineering Solutions of Sandia, LLC.

Available to DOE and DOE contractors from

U.S. Department of Energy
Office of Scientific and Technical Information
P.O. Box 62
Oak Ridge, TN 37831

Telephone: (865) 576-8401
Facsimile: (865) 576-5728
E-Mail: reports@osti.gov
Online ordering: http://www.osti.gov/scitech

Available to the public from

U.S. Department of Commerce
National Technical Information Service
5301 Shawnee Rd
Alexandria, VA 22312

Telephone: (800) 553-6847
Facsimile: (703) 605-6900
E-Mail: orders@ntis.gov
Online order: https://classic.ntis.gov/help/order-methods/

SAND2018-9380
Printed August, 2018
Unlimited Release

Dispersion Validation for Flow Involving a Large Structure

Alexander L. Brown
Erik Benavidez
1532, Fire Science and Technology

Sandia National Laboratories
P. O. Box 5800
Albuquerque, New Mexico 87185-MS1135

Abstract

The atmospheric dispersion of contaminants in the wake of a large urban structure is a challenging fluid mechanics problem of interest to the scientific and engineering communities. Magnetic Resonance Velocimetry (MRV) is a relatively new technique that leverages diagnostic equipment used primarily by the medical field to make 3D engineering measurements of flow and contaminant dispersal. SIERRA/Fuego, a computational fluid dynamics (CFD) code at Sandia National Labs is employed to make detailed comparisons to the dataset to evaluate the quantitative and qualitative accuracy of the model. The comparison exercise shows good comparison between model and experimental results, with the wake region downstream of the tall building presenting the most significant challenge to the quantitative accuracy of the model. Model uncertainties are assessed through parametric variations. Some observations are made in relation to the future utility of MDV and CFD, and some productive follow-on activities are suggested that can help mature the science of flow modeling and experimental testing.

ACKNOWLEDGMENTS

Michael Brown (at Los Alamos National Laboratory) consulted on the design and selection of test conditions for the experiment. We acknowledge the work of the testing team, including Chris Elkins (Stanford), Col. Michael Benson (USMA), and students Nick DiVito, Matt Byers, and Will White. Programmatic support came from the CIESESE internship program, as well as from other programmatic sponsors. Programmatic interest from the Defense Threat Reduction Agency (DTRA), Jon Rogers (SNL), and Michael Clemenson (SNL) were key to the progress and completion of this study. Heeseok Koo (SNL) and Ethan Zepper (SNL) provided helpful guidance key to completion of this activity. Heeseok and Blake Lance (SNL) provided excellent document reviews prior to publication. We are grateful to the testing team (Drs. Elkins and Benson) for providing details on the testing to improve this report in terms of the uncertainties and conditions of the tests, as well as the CAD data images and the contour data images that are shown in comparison to the computational 2D plan images.

TABLE OF CONTENTS

FIGURES

TABLES

NOMENCLATURE

Abbreviation	Definition
CFD	Computational Fluid Dynamics
CFL	Courant-Friedrichs-Lewy
CV	Control Volume
CVFEM	Control Volume Finite Element Method
FFT	Fast Fourier Transform
LANL	Los Alamos National Laboratory
LES	Large Eddy Simulation
MRC	Magnetic Resonance Concentration
MRI	Magnetic Resonance Imaging
MRV	Magnetic Resonance Velocimetry
MUSCL	Monotonic Upwind Scheme for Conservation Laws
PIV	Particle Image Velocimetry
RANS	Reynolds Averaging of the Navier-Stokes equations
SNL	Sandia National Labs
TFNS	Time-Filtered Navier-Stokes
UPW	Upwinding
USMA	United States Military Academy
V&V	Verification and Validation

1. INTRODUCTION

The release of toxic substances into the atmosphere can have adverse effects on the population and environment. With ever increasing population and the variety of activities for which this phenomenology is significant, it becomes increasingly important to understand and predict contaminant dispersion in highly populated areas. Improved understanding can help to mitigate potential negative health and environmental effects.

Contaminants may originate from ordinary sources, such as emissions from vehicles (e.g. Brown and Dabbert, 2003), and exhaust stacks from structures (e.g., Saathoff et al., 2009). Better understanding transport of contaminants from these sources can affect design and construction. Sources may also originate from a deliberate or accidental release of harmful chemical agents (e.g., Heist et al., 2009; Brixey et al., 2009). Understanding how contaminants are influenced by urban geometries can aid government agencies to prepare an emergency response in the event of a chemical attack or unintended release.

The urban environment is particularly challenging because of the complexity of the surface layer. Buildings are constructed in a variety of shapes and orientations. There are a wide variety of arrangements of buildings. There is an effect of the urban structures on the atmospheric boundary layer that is a necessary consideration for bounded domain predictions (e.g. Lateb et al. 2016). The urban boundary layer is significantly different from the rural boundary layer, an effect that is caused by the urban structures. It is typically thicker, extending higher than would be normally expected in a rural or suburban setting. Urban dispersion is often governed by the characteristic length scales in the turbulent urban boundary layer (Lateb et al. 2016; Franzese and Huq, 2011).

Urban structures also can significantly impact the mixing and dispersion in their immediate vicinity, and there has been a focus in the recent literature on scenarios involving a single structure significantly taller than the surrounding structures. Here some specific examples of recent activity are given. Heist et al. (2009) and Brixey et al. (2009) detail scaled wind tunnel experiments and Computational Fluid Dynamics (CFD) simulations that were motivated by a field study of a Brooklyn, NY, USA urban dispersion exercise. They were motivated by findings that the large structure significantly enhanced vertical dispersion in the wake region. Addepalli and Pardyjak (2015) used a wind tunnel with approximately a 1 meter cross-section and a scaled domain to study the effect of a tall structure. Particle Image Velocimetry (PIV) was used to extract planar velocities mostly between a single tall structure and a down-stream structure of varying heights. Hayati et al. (2017) explore simulation comparisons to the dataset using three modeling techniques. Two Navier-Stokes based CFD solvers including Large Eddy Simulation (LES) and Reynolds Averaging of the Navier-Stokes equations (RANS) methods were used, along with QUIC-URB, which uses mass consistency to approximate a flow field. Tominaga et al. (2008) detail working group results from the Architectural Institute of Japan, which focuses on the use of CFD to model the pedestrian wind environment. Several of their characteristic

qualification problems involve tall structures. Pascheke et al. (2008) tested scale wind-tunnel dispersion using naphthalene sublimation and propane point sources with equal-height structure and variable height structure urban configurations. They found the variable height structures contributed to increased lateral and vertical plume spread. Xie et al. (2008) examined flow around variable height structures, and found that the flows were complex and that the tallest structures can have a disproportionate effect on the turbulence in their wakes.

The scenario of a single taller building is challenging because the dispersion (particularly vertical) is enhanced due to the turbulence formed in the wake of the large building. The enhanced dispersion challenges modeling techniques that do not appropriately resolve the turbulent behavior. Such geometry therefore represents a good quality metric for detailed simulation capabilities.

As already noted in some of the above examples, scaling is often used to study large and complex flow geometries that are difficult to study natively. The primary parameter for flow scaling is the Reynolds number, which is the self-similarity parameter relating momentum to viscous forces. In the case of air flow, one studies a smaller scaled geometry at a higher velocity to maintain similar Reynolds number for the flow conditions. Altering the fluid can change density and viscosity, the other two component parameters of the Reynolds number. Flows relevant to large-scale domains can be reproduced at a much smaller scale. Reynolds number matching still results in self-similar results provided that other properties of the fluids are reasonably inconsequential to the flow characteristics. Thus, air flows can, to a first order, be approximated with liquids by maintaining the appropriate scaling and conditional requirements. Regimes where surrogacy might become increasingly questionable would include where compressibility effects become significant, and where density gradients such as thermal variations significantly affect the buoyancy in a flow. The compressibility of air compared to water is significantly different. Froude or Richardson number scaling might be more appropriate and/or significant in some applications of this nature because they include buoyancy effects and density gradient effects. Diffusional effects are often computationally managed through the Schmidt number, which relates viscous and diffusional flow effects. The Schmidt number is also a parameter of interest relating to the self-similarity approximation for turbulent dispersion problems. The Schmidt number may relate to laminar and/or turbulent properties depending on the model assumptions.

A notable example of utilizing a water flow as a surrogate for a gas flow is found in Laskowski et al. (2007). Here, a mixed convection turbulent flow scenario was developed experimentally to study the turbulence and heat transfer from the flow in a water channel with the aim of validating CFD models for heat transfer in a fire application. Richardson number scaling was primarily observed for these flows. The convective heat transport to a cylinder was monitored, having components of natural and forced convection contributing to the heat transfer. Water flow was used as a validation exercise with the intent of using the modeling tools later for gas flow conditions involving similar phenomenology. Experimental data included 2-dimensional PIV and heat flux deduced from thermal measurements around the perimeter of a cylinder in the flow.

The medical field and the diagnostic requirements thereof have led to several well-established non-invasive methods for probing 3-dimensional complex systems. One technique that has thus far had limited application to engineering problems is Magnetic Resonance Imaging (MRI). Elkins et al. (2003, 2004, 2009), Elkins and Alley (2007), Chang et al. (2009), and Benson et al. (2011) detail some of the prior application of the existing technology in the medical industry to flows of engineering interest. MRI equipment uses nuclear magnetic resonance tuned to the hydrogen atom and tomographic reconstruction to extract sub-millimeter resolved concentration and flow information. MRI equipment is scaled for human body interrogation, and because of the strong magnetic fields is limited to materials that are compatible with the environment (non-ferromagnetic). The primary advantage of this technique is the existence of apparatus and post-processing tools to readily interpret test conditions. The technique was recently applied to a series of flow conditions motivated by the atmospheric dispersion literature described above in collaboration with the modeling team at Sandia. A notional geometry was generated to produce flows involving dispersion of a contaminant down-wind of a very tall structure in a mock urban setting. At the time of preparation of this document, the dataset has not been published. A final report on the experimental activities is anticipated in the future (Elkins and Benson), in which case we will cite the corresponding documentation of the test activities.

The presence of detailed scaled data on the flow behavior of a domain motivated by the atmospheric dispersion of contaminants downwind of a tall structure provides the unique opportunity to explore the computational accuracies obtained from simulation tools. The validation exercise circumvents some of the main issues of many of the prior validation exercises. The boundary condition is well characterized in 2-dimensions. The domain results are fully 3-dimensional, and include velocity and concentration time-means. Reynolds number scaling is observed to produce a flow representative of characteristic atmospheric conditions. Comparisons between simulations and data are not constrained to experimentally pre-selected locations of interest. Data exist throughout the domain in scan regions of interest.

This study computationally examines flow and dispersion around a tall building in an otherwise uniform array of cubical buildings. The presence of the one tall building influences significantly the surrounding velocity fields and contaminant dispersion. Comparisons are made between predictions employing a variety of modeling assumptions and the detailed dataset. The results are intended to expose model limitations, characterize expected model accuracy and provide confidence in the ability to simulate dispersion events in a complex flow environment. This scenario was selected because it relates to past studies of similar geometric configurations (e.g., Heist et al., 2009 and Brixey et al., 2009), and is the first of several scenarios expected to be simulated using the combined MRV/MRC and SIERRA/Fuego techniques.

2. METHODS

2.1. Experimental Configuration

This study considers the experimental configuration developed in collaboration with the United States Military Academy (USMA) and Stanford University. Experimental data were collected in a scaled down meteorological EPA wind-tunnel placed inside a Magnetic Resonance Imaging machine. The upstream section of the water channel is composed of roughness layers and a Counihan vortex generator designed to generate turbulence and simulate atmospheric conditions before reaching the test section. Roughness layers included an array of Lego ™ blocks arranged uniformly on the floor of the channel. The test section was printed using a 3D print technology, and the same geometry representations delivered to the printing systems could be adapted to generate the computational meshes of the flow area. The 3D printing was a 3D Systems Viper Stereolithography machine with an Accura 60 resin from 3D systems. The resolution was 0.004 inches in the x/y plane with 0.010 inch layers.

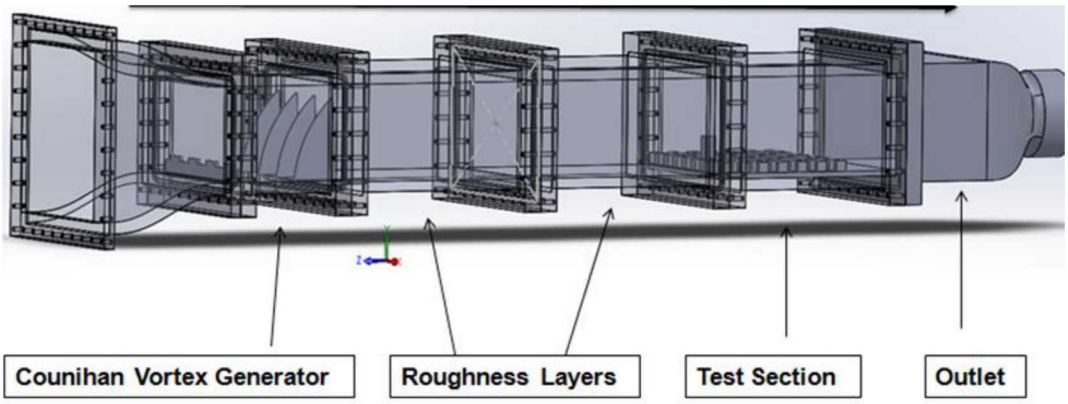

Figure 1. Water Channel Design

The test domain was proposed by Mike Brown (Los Alamos National Laboratory, or LANL), who was a participant in some of the past studies on atmospheric flow described in the introduction (and based on prior detailed literature). The test section was manufactured from a non-ferrous resin using stereolithography. It is 196 mm wide, 110 mm high and 239 mm long (internal flow dimensions). The mock buildings are arranged in an evenly spaced 7×9 array. The uniform cubical buildings have a characteristic length of L=12.25mm. The tallest building is of the same length and width and with a height of 36.75mm, three times that of the surrounding structures (3L). The gap between the buildings is the same characteristic length (L). The tall building is centered in the x-direction, and in the second row of buildings in the z-direction (flow direction). The contaminant injection site is located immediately downstream of the tallest building. The contaminant is injected directly into the water channel through holes drilled over the top of a 12.25 mm x 12.25 mm injector located down-stream of the tall building at the channel floor. The contaminant, an aqueous solution of $CuSO_4$, is injected at a low constant flow rate of 0.4L/min compared to a

bulk flow rate of 410L/min. This was done to limit the disruption of the bulk flow by the contaminant injection. Concentration measurement resolution limitations exist, so multiple tests were simulated with different contaminant concentrations. The resultant data were scaled and stitched together to give a more comprehensive range of contaminant measurements. The baseline specific gravity of the aqueous solution was 1.003, and an elevated specific gravity was employed for higher resolution data (1.015). There are not expected to be significant density variations and buoyancy effects in the tests, as density variations are minimal. The water was maintained at a constant temperature of 21°C throughout testing. The entire test section was scanned by the MRI machine to collect average velocity and concentration data. Scans were conducted immediately upstream of the buildings to collect initial condition data for numerical simulations at the interface between the test section and the roughness layer section. During Magnetic Resonance Concentration (MRC) measurements, a waste water reservoir was incorporated to prevent the concentration of contaminant in the bulk flow from rising over time as would occur if recirculation were used.

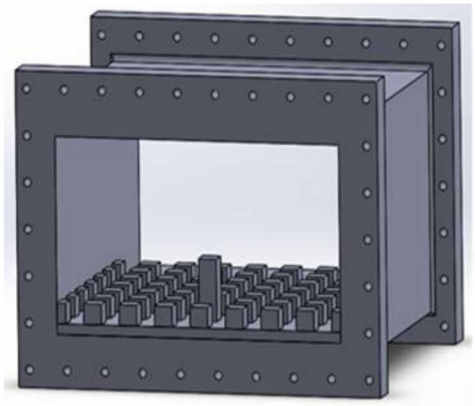

Figure 2. Test Section Geometry Image

The MRI technique (MRV and MRC) is able provide a data resolution of 0.8mm. Such resolution data exist throughout the test section, however in this comparison effort only a subset of the experimental data are evaluated primarily via detailed line comparisons. The rich nature of the data is not typical of CFD validation comparison studies. There seems to be need for methods to be developed, discovered, or identified (if existing in other fields) that can be used for more comprehensive validation comparisons between the 3D simulation and the 3D experiment results. Data accuracies have been assessed, and preliminary estimates suggest the velocity data are accurate to 6%, and concentrations to 4%. These were provided by the test team, and it is expected that final figures will be independently documented and detailed by them in an independent forthcoming publication.

The CAD geometry from the test design team was passed to the modeling team. The fluid mesh was constructed from the same geometry file that was used to generate the 3D prints of the domain for the flow experiments.

2.2. Numerical Configuration

Sierra/Fuego, a low-Mach CFD code developed by Sandia National Laboratories, was used to conduct simulations (Sierra, 2017a and 2017b). Sierra is a general architecture for engineering computational tools developed and maintained at Sandia National Labs. Fuego is the low-Mach number CFD solver initially designed to predict fire behavior and conjugate heat transport to objects in the fire. It is particularly distinguished from other current fire CFD solvers in common use in that it is a control volume finite element method (CVFEM) formulation rather than a pure control volume (CV) method. The code is massively parallel, and inherits the solver and numerical packages developed for Sierra which are aimed at supporting and leveraging advanced capabilities of evolving computer hardware. Fuego couples to other multi-mechanic codes in the same Sierra framework, however this capability is not necessary for this exercise. The solver is a segregated solver, and sequentially solves the governing continuity, momentum, turbulence, and mixture fraction equations. Within a timestep, the segregated solver would repeat for Time-Filtered Navier-Stokes (TFNS) and k-ε simulations to achieve improved timestep convergence.

All calculations for this study were performed with version 4.46.2 of the code, and simulations were run on a variety of the current high performance clusters at Sandia National Labs. Corresponding documentation can be accessed for the equation set solved. No unique model variations were employed for this study.

2.2.1. Domain and Grid Size

The numerical domain is modeled based on the nominal conditions created for the experimental program, the CAD file that was used to 3D print the geometry for the tests. The simulation domain is 196 mm wide, 110 mm high and 239 mm long. The computational domain is composed of hexagonal grid elements of varying size. A horizontal and vertical mesh bias scheme was utilized to yield a less computationally expensive domain with tapered mesh relaxation outside the region of primary interest. The inlet and outlet boundary conditions were placed more than H, the height of the tallest building, away from the edge of the buildings to avoid artificial acceleration near the boundaries. A grid sensitivity study was performed to demonstrate solution convergence. Three meshes were generated to examine the solution sensitivity to mesh size (coarse, medium, fine). The coarse mesh contained 1.0 million cells with a resolution high of 1.5 mm. The medium mesh utilized a localized grid refinement closest to the target building yielding a local resolution of 0.5mm and 3.6 million elements overall and was considered the baseline mesh during the parameter sensitivity study. The fine mesh contained 14 million elements and a local resolution of 0.375mm closest to the tall building. Figure 3 (left) shows the mesh for the baseline LES scenario. The $CuSO_4$ injection area is white in the surface structure plot. The time step for each mesh was determined by the smallest cell size. The time step was adjusted for each consecutive refinement such that the Courant-Friedrichs-Lewy (CFL) number did not exceed 0.5. A fixed timestep was used. This helped assure stable flow, and provided a timestep consistent with the resolved flow on the mesh. Table 1 summarizes mesh and timestep model parameters for simulations run for this study.

Table 1. Mesh and timestep details for simulation cases

Mesh	Cells (million)	High Resolution (mm)	Cases	Timestep (s)
Coarse	1.0	1.5	k-ε, LES (1)	0.0015
Medium	3.6	0.5	TFNS, LES (all others)	0.0005
Fine	14.0	0.375	LES (1)	0.0003125

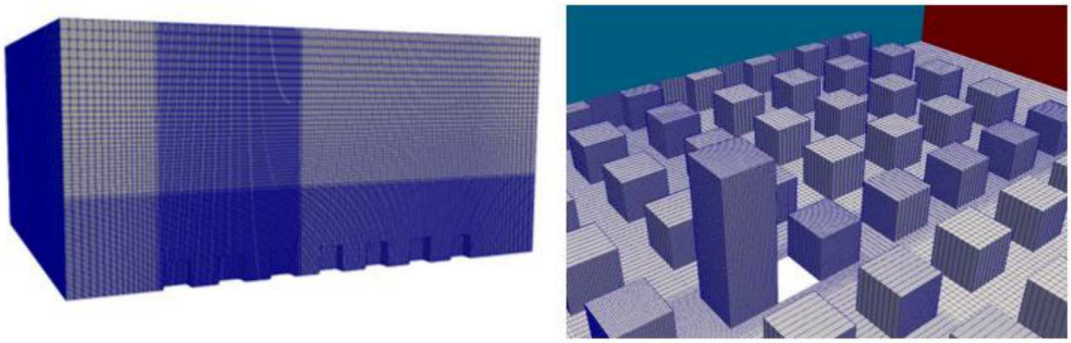

Figure 3. The Medium Mesh from the Outer Boundary (left) and at the Structure Surfaces (right)

A consistent coordinate system is used throughout this report. The z-direction is the direction of flow, and the flow is in the negative direction. The y-direction is vertical. The x-direction is span-wise. This is consistent with the coordinate system from the CAD model as drawn in Figure 1.

2.2.2. Turbulence Models

This study examined the performance of multiple turbulence models. The turbulence models considered for this study were k-ε, LES and TFNS. The aim of this study is to compare the results of different turbulence models and model parameters in comparison to experimental data and evaluate the accuracy of SIERRA/Fuego for applications of dispersion for urban flow geometries.

k-ε is a relatively inexpensive RANS method for simulating flows and is widely used in engineering applications. It was conceived in the 1960-1970 timeframe, and is meant to simulate scenarios with insufficient resolution to resolve the turbulent scales (e.g. Launder and Spalding, 1983, Jones and Launder, 1972). The standard k- ε model is a two-equation method which solves turbulent kinetic energy and rate of turbulent dissipation numerically through transport equations and treats turbulent viscosity as isotropic. Dispersion is related directly to the turbulent viscosity, which is augmented due to the increased dissipation modeled in the eddy dissipation. Thus, dispersion at the sub-grid scale is heavily linked to the turbulent parameters.

LES applies a spatial filter to the turbulent equations, resolving turbulence at the grid level and modeling sub-grid turbulence. Dispersion is primarily advective as resolved on the grid, with a lesser fraction of the dispersion relating to the turbulent viscosity through the sub-grid model. In our case, we utilize the KSGS model (Kim and Menon, 1997). A single equation turbulent kinetic energy model is used to simulate the sub-grid turbulence.

Time-Filtered Navier-Stokes is a hybrid method containing aspects of LES methods and standard RANS models. TFNS applies a time filter to limit the sub-grid scale turbulence. It bases the sub-grid scale on the standard k-ε model (Tieszen et al., 2005). It has been used mostly in the past at Sandia National Labs (SNL) for fire simulation applications, and to our knowledge is not widely adopted in the CFD community. Dispersion depends on the turbulent viscosity at the sub-grid level. Advective dispersal is resolved to the temporal filter. In the case of these simulations, the magnitude of the temporal filter selected was two times the timestep.

2.2.3. Mixture Fraction Approximation

A mixture fraction approximation was applied to model the contaminant dispersion throughout the numerical domain. The mixture fraction is the ratio of the amount of injected flow present in the bulk flow to the bulk flow. A transport equation for scalar mixture fraction was used to model the dispersion of the contaminant. Constant properties with the surrounding water flow were assumed. This means that no buoyancy effects were resolved in the simulation. Buoyancy effects are anticipated to be negligible, as concentrations were insufficiently large to change the density by more than a few percent.

Because both the experiment and model were optimized to give concentration levels in stream fractional magnitudes, we represent concentration in this way for the remainder of this report. Concentration for this study is therefore unitless, and represents more accurately stream mass fraction subject to a constant density approximation.

2.2.4. Boundary Conditions

MRV data were collected immediately upstream of the building array to provide velocity data to apply to the inlet boundary condition in the numerical model. Several functions that involved step-wise interpolation of the inlet data from the experiment were applied to capture the behavior of the inlet velocity profile. Each function generated from the experimental data described how the velocity of the inlet plane varied in the horizontal direction and was applied to a specific range in the vertical direction corresponding to the equivalent range in the experimental data. The baseline case contained 20 functions. Figure 4 shows a graphical contour plot comparison between the numerical inlet velocity profile as applied in the models versus the measured experimental inlet profile. The inlet profile was a reasonable approximation of the experimental condition. Stream-wise velocities from the experiments were applied at the inflow boundary. The other velocity components were relatively small, and omitted (assumed zero) in the simulation boundary conditions. An example input file is shown in the appendix, which contains the details of the step-wise inflow

boundary condition functions. The MRV data consisted of average flow conditions during the test, and lacked any fluctuations.

Because of the perforated plate and presumed pressure drop across the boundary, the contaminant injection site was assumed to be a single uniform bulk flow over a flat surface at the bottom of the water channel floor. The fixed velocity condition was 0.044 m/s, and the turbulent kinetic energy was assumed to be low (1e-6 m^2/s^2). All incoming flows were isothermal at a temperature of 21°C with a constant density and viscosity.

A.

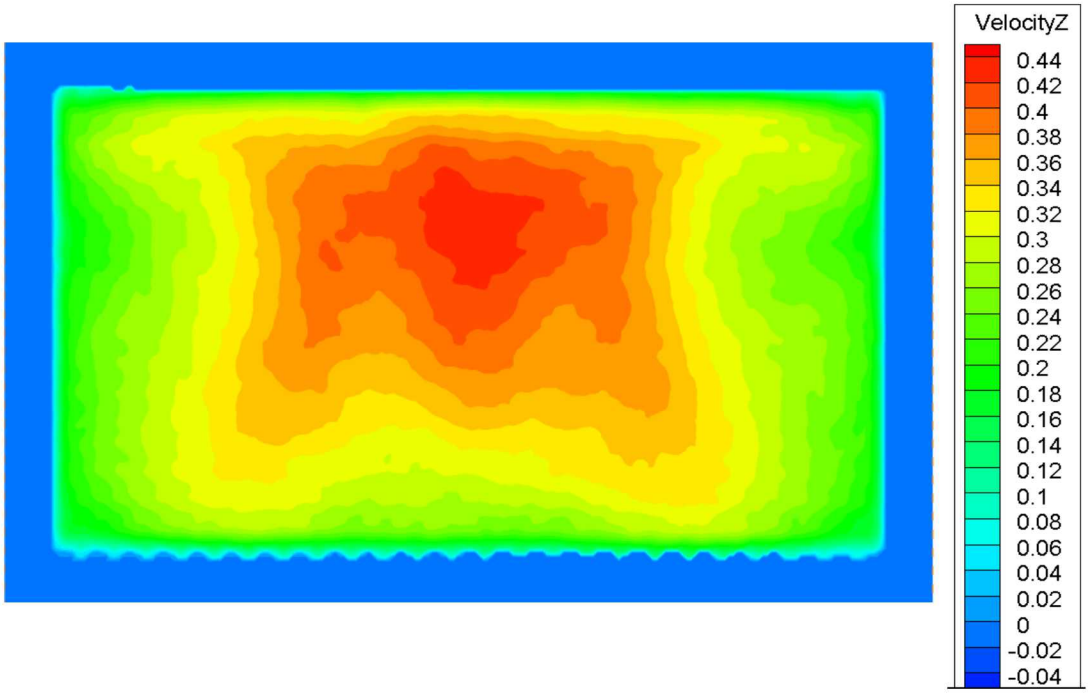

B.

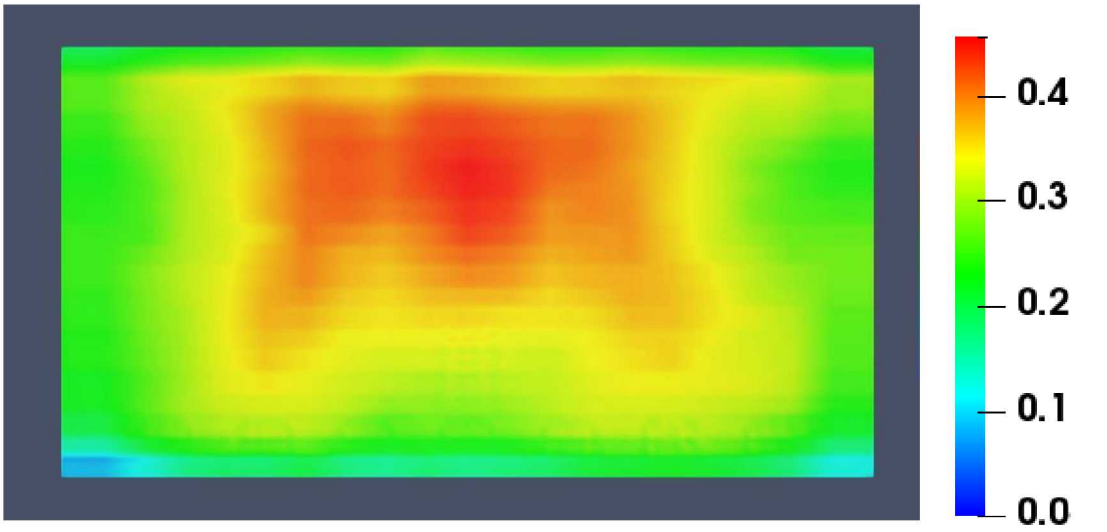

Figure 4. Inlet Velocity (m/s) Comparison (x-y plane)

The walls and buildings within the simulation were treated as smooth walls with a no-slip condition applied. Wall functions were utilized to simulate the viscous effect of a developed turbulent boundary layer at the location of the wall in the first node perpendicularly above the flow. The adequacy of this assumption is discussed later, and y-plus values relevant to the boundary layer approximation are described for some of the resulting simulations.

2.3. Parameter Sensitivity

A parameter sensitivity analysis is intended to assess numerical model sensitivities. Through this, it is intended to provide insight on the numerical uncertainty related to modeling assumptions in relation to the LES turbulence model. Table 2 shows the main parameters of interest and the changes that were made with respect to the baseline simulation. Meshes with systematic resolution refinements were examined. The baseline time-step ensured that the CFL number did not exceed 0.5, while larger time steps corresponding to CFL limits of 0.75 and 1.0 were also considered. The inflow sub-grid scale turbulence intensity was increased by 5% intensity over five iterations. A higher order discretization scheme, standard upwinding (UPW) and Monotonic Upwind Scheme for Conservation Laws (MUSCL; van Leer, 1979), was examined as well as variations in first order and hybrid unwinding factors (0.0 or 0.001). The linear residual tolerance was lowered by an order of magnitude of each case to examine solution convergence. The laminar Schmidt number was varied according to magnitude differential values motivated by previous research (Shen et al., 2017). The number of velocity inlet functions and resolution was increased, in order to assess the accuracy of the functions created to model the experimental velocity behavior. Experimental conditions with inherent uncertainty, temperature and contaminant injection rate, were also examined. Because the energy equation was not solved for this case, the temperature was modified by adjusting the density and viscosity based on literature information. This included about a 0.1% change in density, and 10% change in viscosity.

Table 2. Parameter Study Details

Variable	Type	Baseline	Variation
Mesh Refinement	Numerical	Medium	Coarse, Medium, Fine
Time Step	Numerical	.0005s	+150%, +200%
Turbulence Intensity	Experimental	0%	+5%, +10%, +15%, +20%
Upwind Scheme	Numerical	UPW	UPW factors, MUSCL
Residual Tolerance	Numerical	1E-5	$x10^{-1}$, $x10^{-2}$
Schmidt Number	Experimental	0.9	0.7, 0.5 (Literature Values)
Inlet Velocity Profile	Experimental	20 functions	Function accuracy, number of functions
Temperature	Experimental	21°C	±5°C
Contaminant Injection Velocity	Experimental	4.4 cm/s	±10%, ±20%

3. RESULTS

3.1. Planar and 3D comparisons

Figure 5 compares the contour plots of concentration at the center of the domain in the stream-wise direction. The comparatively smooth LES simulations are characteristic of simulation results, and represent the time-averaged predictions once statistically stationary results are obtained. There are artifacts in the data that occur along a curved line that corresponds to the stitch points for the two concentration datasets. These are probably attributable to the regime of accuracy issues with the data, and may be enhanced as an artifact of the visualization software. Variable and non-continuous effects should be ignored.

Aside from the two prior observations, there is quite good comparison between the data and model. Looking at major color contour transitions, they appear to be well collocated. Trends and magnitudes are reasonably similar. The top of the high building exhibits concentration in the simulation results, whereas the data suggest negligible concentration at that location. This could be a data sensitivity issue, and not as much a difference between model and experiment. Concentrations are very low in that region.

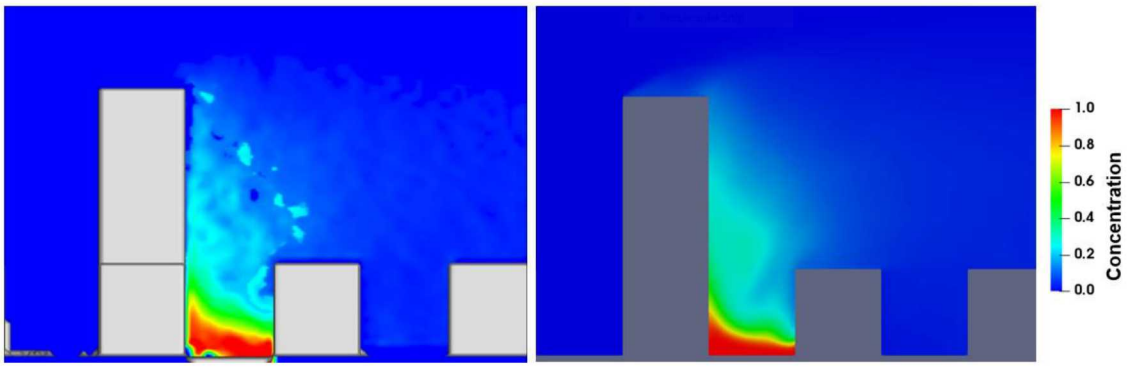

Figure 5. Center-Plane Stream-Wise Comparison Between Experiment (left) and baseline LES (right) (z-y plane). Wind is from the left to right

Figure 6 shows contaminant iso-surface comparisons at various concentration levels. Comparisons were made at 20%, 40%, 60% and 80%. Each surface demonstrates how the contaminant is dispersed and behaves at different concentration levels. Streamlines are also shown, which were released from the line interface between the tall building and the contaminant injection. The model and data produce similar stream behavior with minor differences in the wake of the building and in recirculation flow at the sides and top.

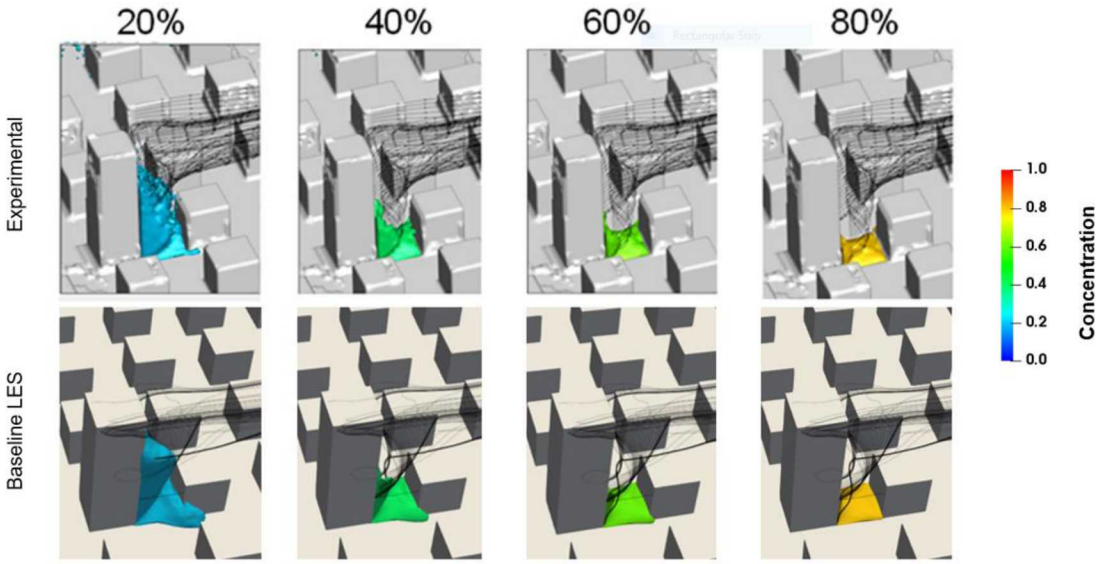

Figure 6. Concentration Iso-Surfaces and Stream-Lines, Oblique View

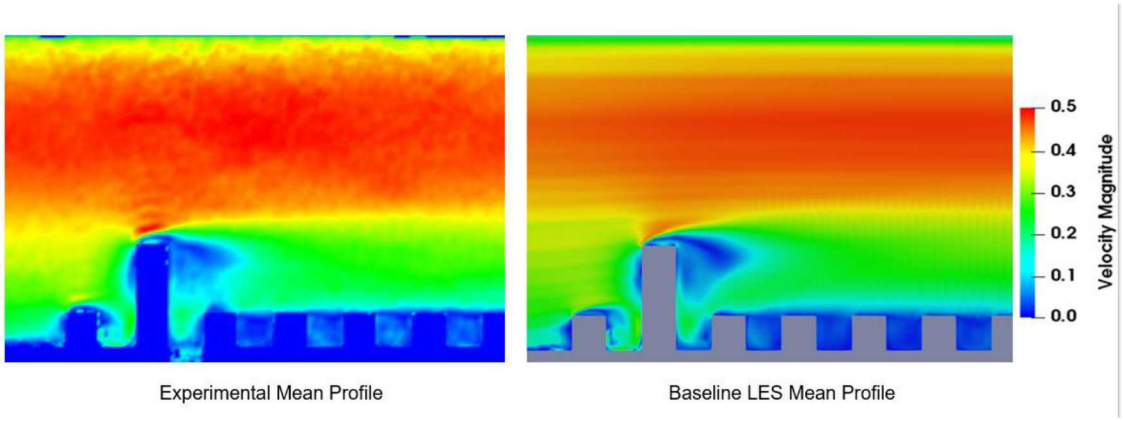

Figure 7. Center-Plane Velocity Magnitude Contour Plots (y-z plane). Wind is from left to right

Figure 7 illustrates the velocity contour plots comparing the experimental velocity magnitude to the results obtained by the baseline LES simulation. The velocity magnitude comparison plots demonstrate a good qualitative match and demonstrate that the flow features are strongly influenced by the tall building. A good overall quantitative match also appears to exist. Quantitative differences appear subtle. Figure 8 shows horizontal plane concentration contour comparisons. The qualitative comparison is reasonably good, with a slightly wider dispersion at very low concentrations shown in the simulation results at 5/6H and 1/6H, H being the height of the tall building. The data are not particularly accurate at low concentration values, so it may not be a significant difference.

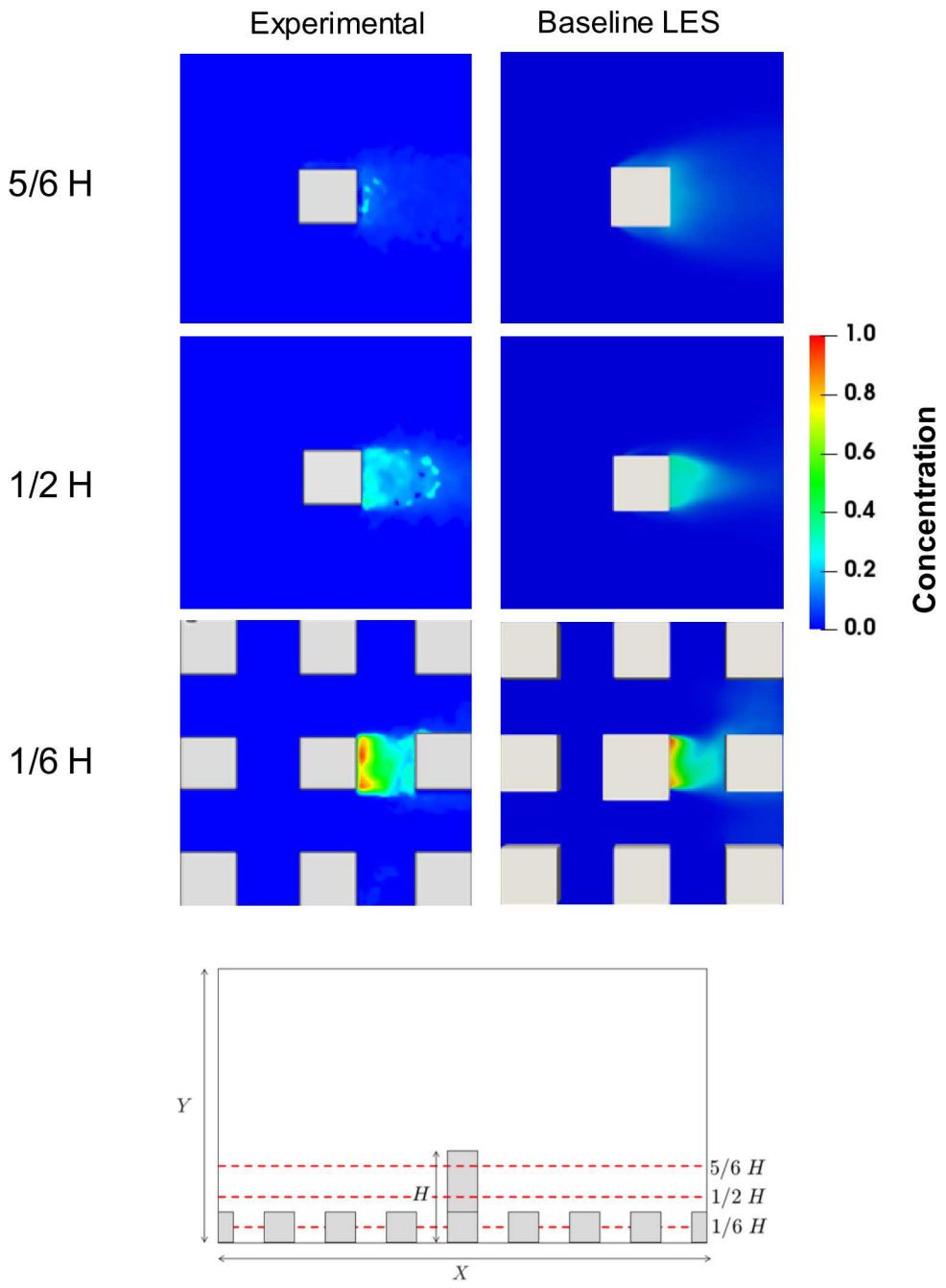

Figure 8. Concentrations at Various Elevations (expressed as a fraction of the height of the large building) with Images Centered on the Tall Building (x-z plane). Wind is from left to right

Figure 9 shows a concentration comparison in the middle of the street canyon where the release occurs. There are minor differences in the low plume region (height of the red contour), and shape of the mid-height concentrations (green-blue transition, concentrations in the 0.2-0.4 range). The outline and general shape is similar between model and experiment.

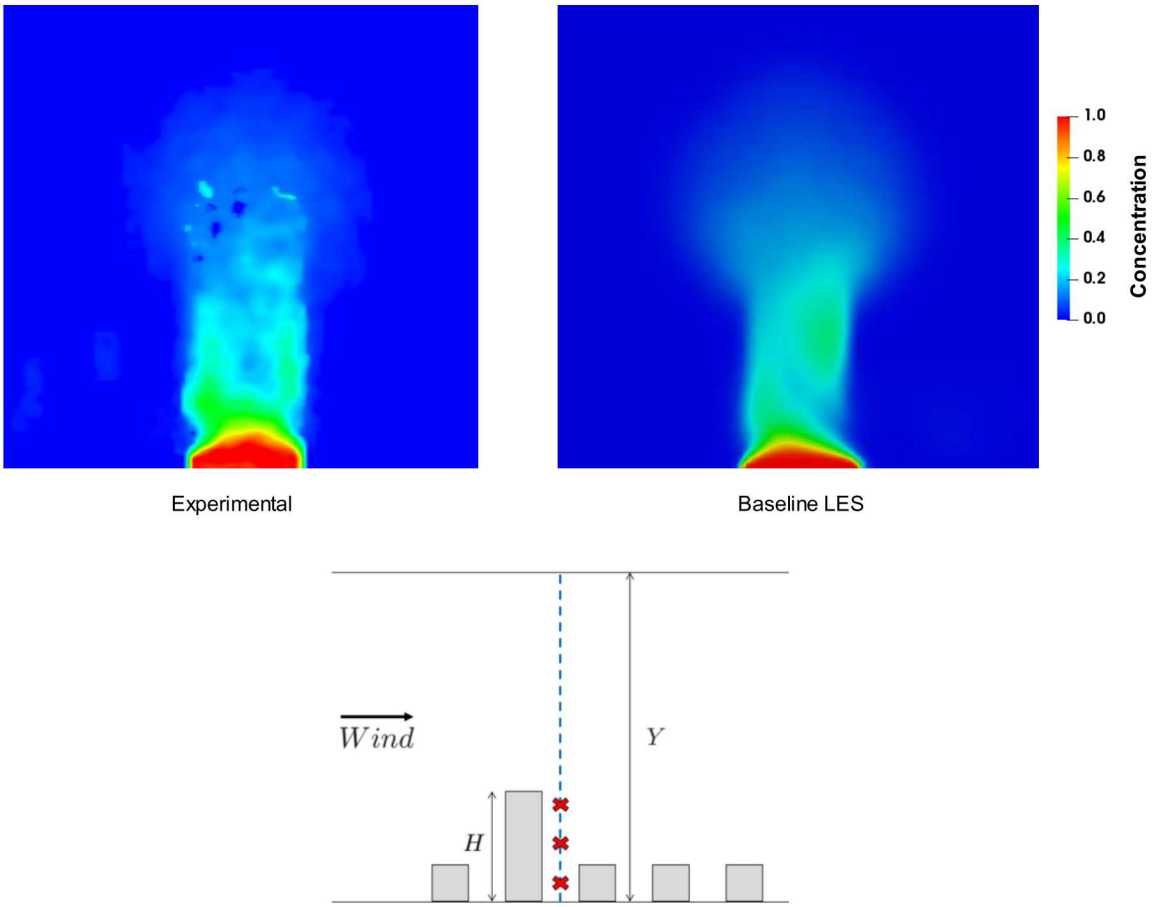

Figure 9. Concentrations in the Street Canyon Where Release Occurred (x-y plane)

3.2. Line Comparisons

For illustrating detailed results, lines have been selected over which to extract data and model results. Because of the richness of the dataset, locations were selected aligning with all of the coordinate directions. Figure 10 shows detailed predictions from the simulations. A uniform representation is used for all line plots. Data are plotted with black square markers, TFNS model results with blue triangles, and coarse results with red dashed lines. All others are the colored lines, showing a relatively tight distribution of results from the parameter study. Stream-wise comparisons were made at the center of the domain (laterally) and at varying heights within the target street canyon of length L. Comparisons were made near the 1/6H, 1/2H, and 5/6H, where H is the height of the tall building. The coarse LES results were outliers in the 5/6 H elevation results. The k-ε results best quantitatively matched the data at l/L > 0.2 for 5/6 H and 1/2 H. Below 0.2 l/L, the TFNS and LES simulations were a better quantitative and qualitative match to the data. The 1/6 H results for LES and TFNS better matched the data, although there were some differences at l/L >0.8.

Because of the numerous results obtained from the test matrix and the fact that there were few outliers, the parametric variations in the LES results were taken to be

representative of the numerical uncertainty. They were assumed normally distributed, and henceforward the LES results are represented by a mean and an estimated 95% confidence interval range over which LES simulations were realized. This was based on 1.96 times the standard deviation of the baseline and baseline variant simulation realizations.

Figure 11 shows the measured experimental concentration and velocity magnitude and the corresponding simulation values in the stream-wise direction plotted against the normalized street canyon length. This plot includes the simplified illustration of the LES results. This provides a clear visualization of the overall average outcome and the degree of variation between simulations. Concentration results for TFNS and LES were reasonably close to the data for these lines, although the LES uncertainty bounds did not capture the data by a small amount for various heights and stream-wise distances. The k-ε concentration result were significantly higher than the data.

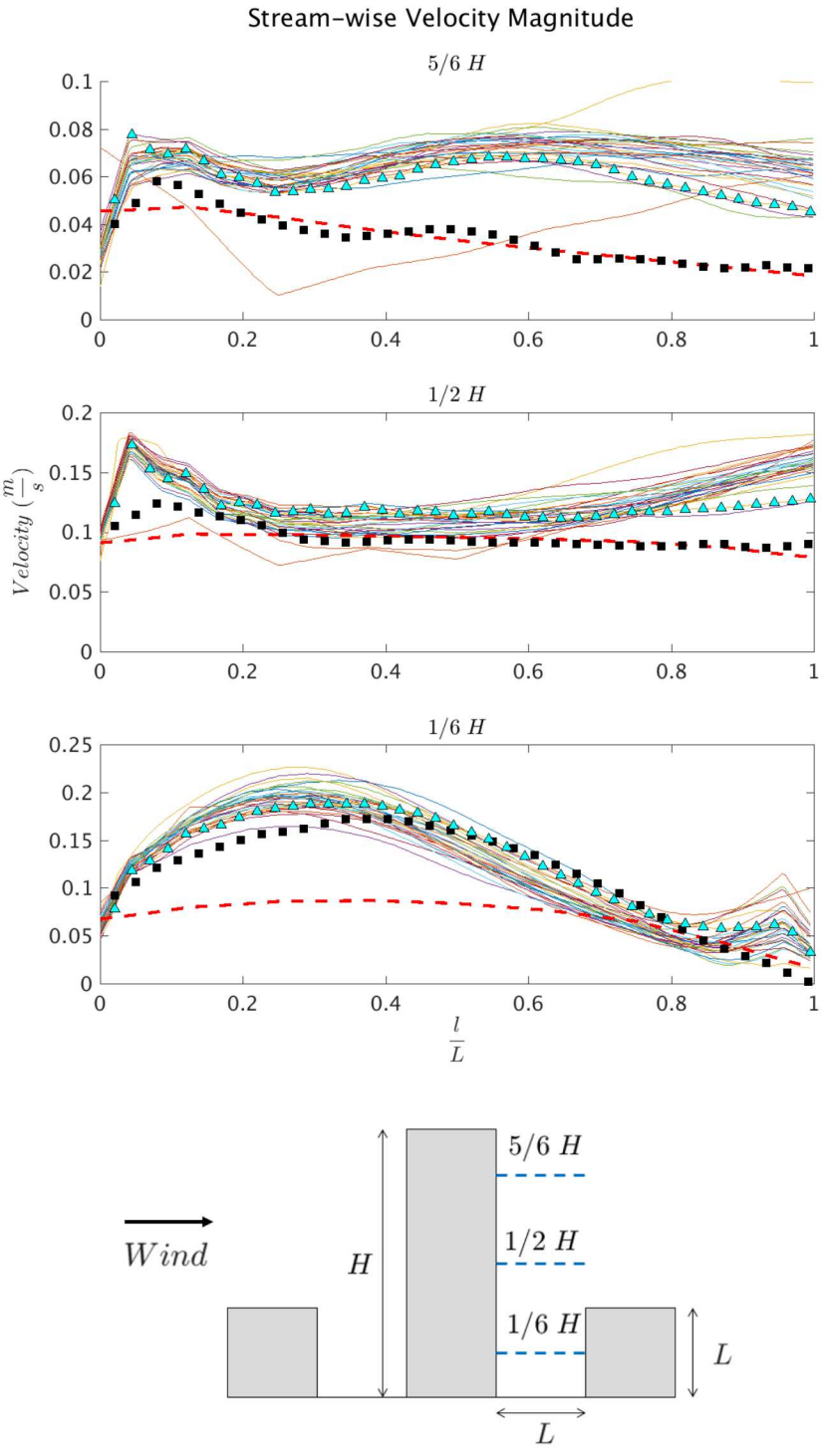

Figure 10. Full Results of Stream-Wise lines of Velocity Predictions at Three Heights

Plots of individual velocity components for the stream-wise direction are found in Figure 12. The LES and TFNS predictions that were generally higher than the data for 5/6H and 1/2H are here shown to be higher principally because of the y-component (vertical) predictions. Z-component predictions are slightly greater in magnitude too

for 5/6H (although negative), while x-component predictions and data all agree on values close to zero. At 1/2H, the y-component velocities appear to be the most significant to the magnitude accuracy. At 1/6H, the y- and z- component velocities for TFNS and LES match the data well, while x-velocity trends differ. The main source for velocity magnitude disagreement with data for k-□ appears to come from the z-component.

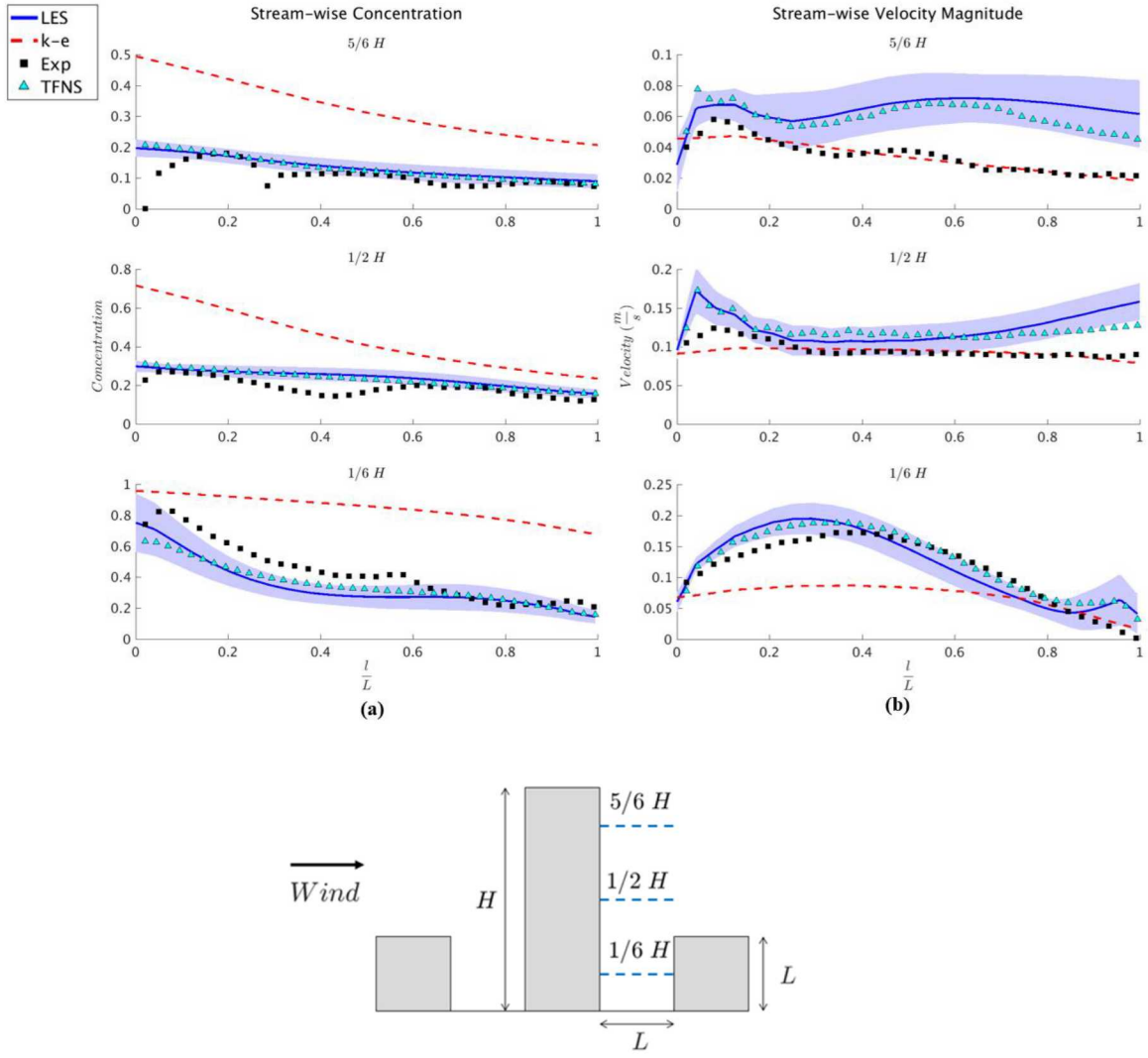

Figure 11. Stream-Wise Concentration (a) and Velocity Magnitudes (b) at Various Heights (c) Within Target Street Canyon

Plots of velocity components for the span-wise directions at varying H are represented by Figure 13. The z-velocity predictions match closely the trends of the magnitude data. The general data trends are observed in the other component predictions with minor differences in magnitude predictions versus the data.

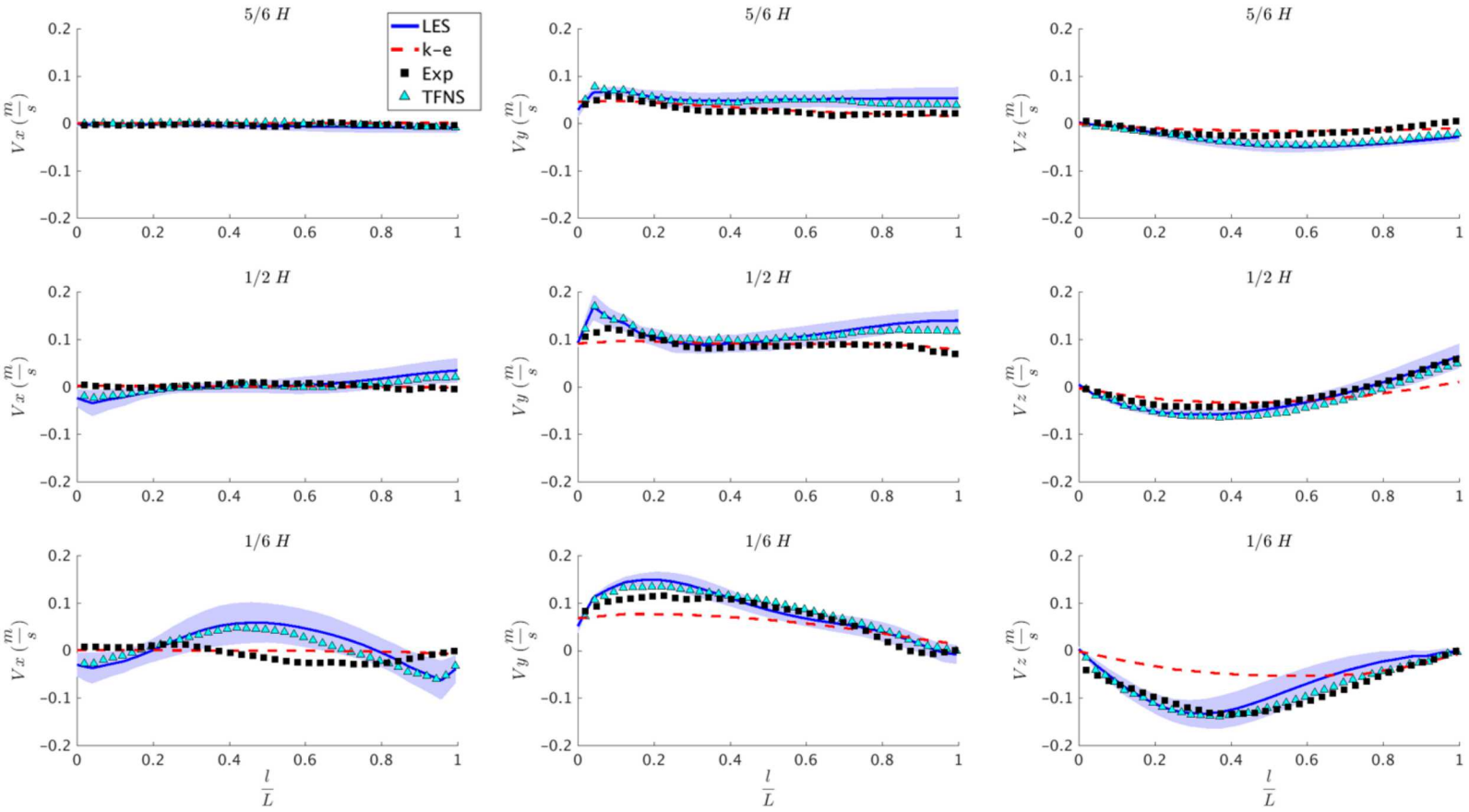

Figure 12. Stream-Wise Velocity Components at Various Heights Within Target Street Canyon

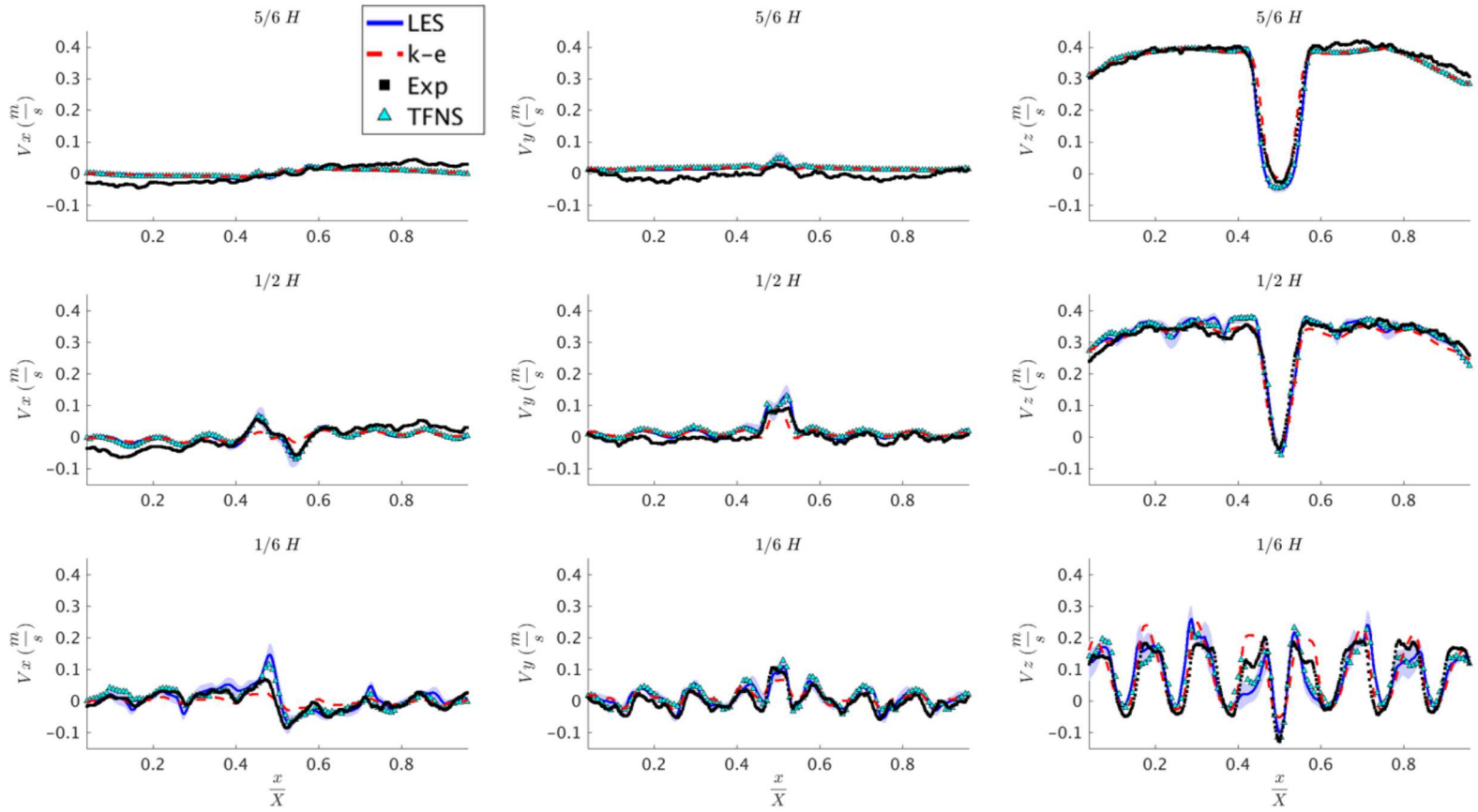

Figure 13. Span-Wise-Wise Velocity Components at Various Heights Within Target Street Canyon

Comparison plots were also generated beyond the target street canyon to observe the long-term stream-wise concentration and behavior. Such plots include results from the prior plot (Figure 11), but extend further. They are found in Figure 14. Comparisons were only extracted for heights 1/2H and 5/6H due to presence of the small buildings at low H. Comparisons extend to 8 building lengths away from the lee-ward face of the tall building to visualize the downwind behavior. While the k-ε model exhibited good comparisons with the data in the region nearest the large building, progressing away from the building, the model significantly under-estimates the velocity magnitudes. Improved comparisons are found to the LES and TFNS model predictions at 5/6 H. At 1/2 H the results are qualitatively similar, but exhibit the inflections at different z/L distances. The free-stream magnitudes tend lower than the data at longer distances downstream.

Line plots of experimental and numerical velocity magnitude and concentration values in the span-wise direction in the middle of the release street canyon are presented in Figure 15. These correspond to the vector component plots already presented in Figure 13. Concentration and velocity magnitude values are plotted against the normalized channel width and compared near the bottom, middle and top of the tallest building. The velocity magnitudes at 5/6H are relatively consistent among all models. The 1/2H results are very good also, with the 0.4 x/X results showing moderate differences between TFNS/LES and the k-ε/data groupings. The k-ε model predicts a slightly wider drop in velocity magnitude around 0.5 x/X. Predicted velocity magnitudes at 1/6H are respectably close to the data. Major trends are mostly reproduced except the k-ε model between 0.4-0.6 x/X. Magnitudes of velocity between buildings are relatively well reproduced, and also exhibit a wide spread in the modeling uncertainty. Concentration predictions are quite good for TFNS and LES, especially at 5/6H. At 1/2H and 1/6H, the model results and data are just outside uncertainty bounds. The major trends are identical, suggesting qualitative accuracy. The k-ε model significantly over-predicts peak concentrations at x/X=0.5, and produces a narrower spread at 5/6H.

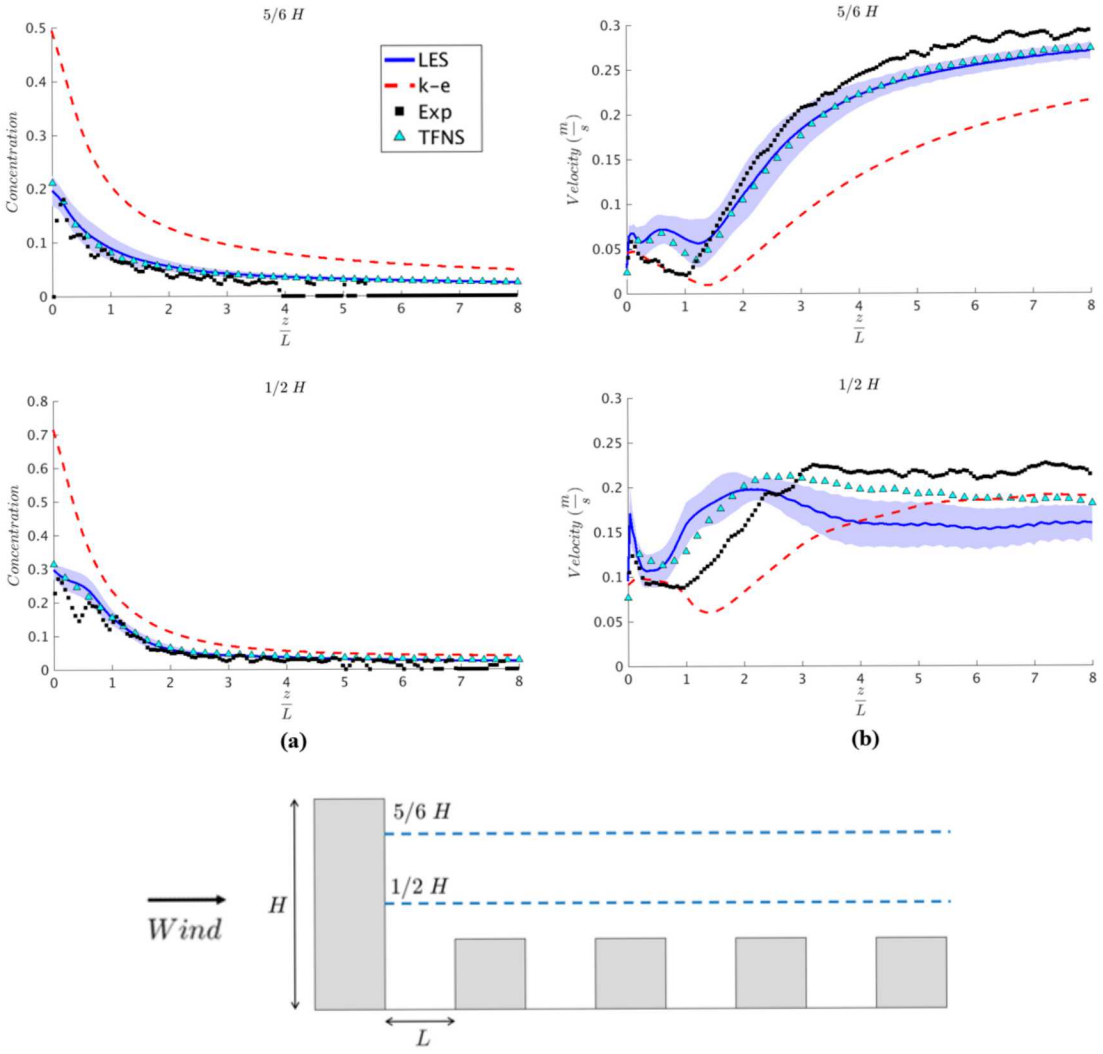

Figure 14. Stream-Wise Concentration (a) and Velocity Magnitudes (b) at Various Heights within Target Street Canyon

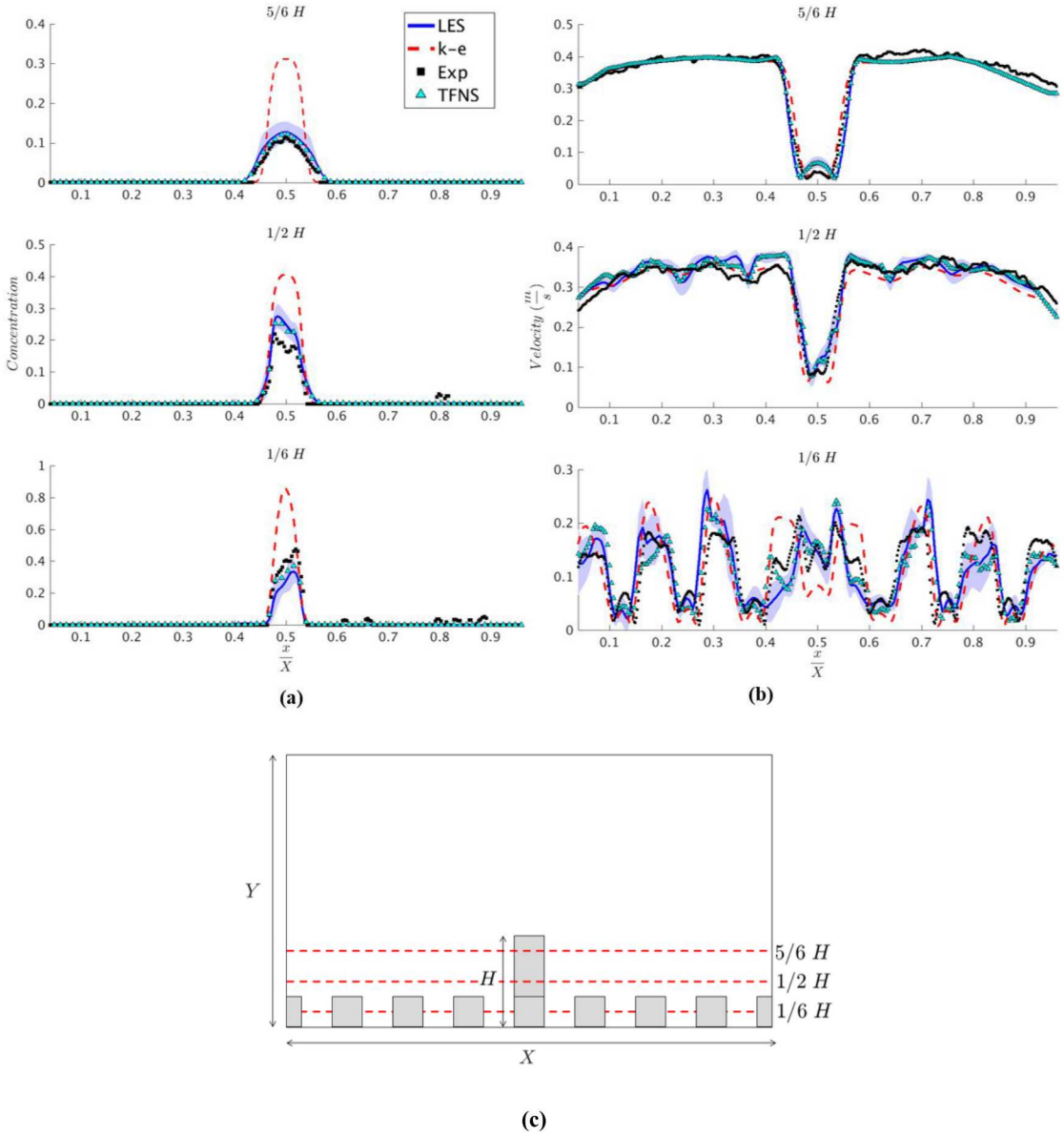

Figure 15. Span-Wise Concentration (a) and Velocity Magnitudes (b) at Various Heights (c) Within Target Street Canyon.

Vertical-direction comparisons were made from the center of the injection site toward the roof of the channel. Velocity and concentration values are plotted against the normalized channel height. These results are shown in Figure 16. The top of the tall building is at y/Y=0.33, and both concentration and velocity data show major inflections in the data around that point. Concentrations go to zero shortly thereafter, and the velocity magnitude increases quickly to a free-stream condition. The inflection point in the velocity magnitude is off by a small distance for the TFNS and LES predictions. The k-ε model agrees with the data more closely in this respect. Velocity magnitudes are reasonably well predicted by the TFNS and LES models otherwise, while the k-ε model predicts lower velocities for low y/Y < 0.2. The TFNS and LES models compare well to the concentration data, while the k-ε model significantly over-

predicts concentration magnitudes below 0.4 y/Y. The high concentration predictions for the k-ε model probably relate directly to the significantly lower velocities predicted in the wake region behind the tall building.

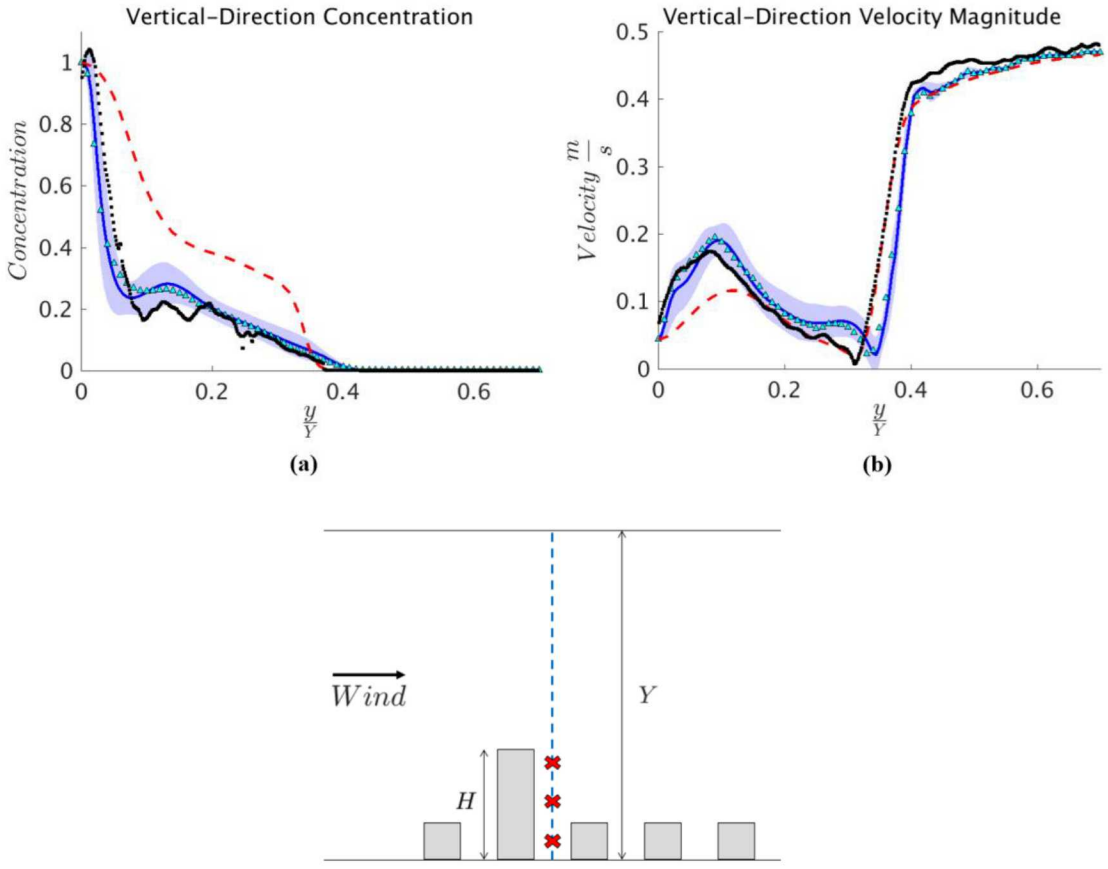

Figure 16. Vertical Direction Concentration (a) and Velocity Magnitude (b) Line Plots

3.3. Point Comparisons

The plane and line comparisons do not represent the full richness of the output from the comparisons. Points in space were selected at which to track the dynamic species concentration and velocities. These points are the familiar 1/6H, 1/2H, 5/6H elevation locations at the x center plane and positioned in the z-direction directly between the tall building and the next down-wind building. Table 3 adds to what has already been presented at these locations by showing the temporal mean and standard deviation from the simulations. Temporal mean is calculated consistently as was the data. Mean component velocities were determined, and then a mean vector magnitude constructed from the mean vector components (as opposed to mean magnitude at each timestep then averaged). The standard deviation is based on the mean magnitude from every

timestep, and is smaller than if derived by taking the magnitude of a standard deviation vector from the components. The TFNS and LES baseline simulations predict a significant variability at these three locations. Taking into consideration the large relative magnitude of the standard deviation, the differences in predicted mean velocities between the data (as much as 2×) don't look as poor. The magnitude of the fluctuation variability is high compared to that of the bounds estimated from the parametric sensitivity study for the LES model parameters. The k-ε model does not exhibit appreciable temporal variability, which is expected based on the nature of the model. The fluctuations are damped by the turbulent and artificial viscosity, and the advective effect of the eddies is modeled through the turbulent diffusivity.

Table 3. Centerline l/L=0.5 flow statistics (mean, μ, and standard deviation, σ) at the three selected heights based on 5-20 second predictions

		5/6H		1/2H		1/6H	
Case	**Variable**	μ	σ	μ	σ	μ	σ
Baseline LES	V-mag (m/s)	0.0733	0.0510	0.1077	0.0760	0.1386	0.0658
	Concentration	0.1237	0.0564	0.2562	0.1038	0.2780	0.2035
TFNS	V-mag (m/s)	0.0652	0.0474	0.1151	0.0474	0.1607	0.0695
	Concentration	0.1231	0.0470	0.2351	0.0796	0.3147	0.1545
k-ε	V-mag (m/s)	0.0334	0.0	0.0959	0.0	0.0836	0.0
	Concentration	0.3121	0.0	0.4070	0.0	0.8605	0.0
Data	V-mag (m/s)	0.0316		0.0876		0.1586	
	Concentration	0.1306		0.2507		0.2975	

These point comparisons suggest the LES and TFNS model have significant variation from the data values, with the peak variations occurring at 5/6H for the velocity magnitude. While differences here are higher than a factor of 2, looking back at the line plots (e.g., Figure 15) the variation does not appear as significant due to the relatively small velocity magnitudes at that point, and the generally positive agreement between data and models on linear trends.

The experiments did not result in data more than the mean values of concentration and velocity. Thus, there is insufficient information to deduce the temporal standard deviation of these parameters. Significant digits in Table 3 should not be taken as accuracy, which is quantified in other ways in other parts of this study.

4. DISCUSSION

The richness of the dataset produced by the MRV/MRC technique allows for very detailed comparisons between the experiments and simulations. Simulations normally have high fidelity, and significant components of the simulation predictions are typically omitted from validation comparison exercises. This report omits significant amounts of both model and experimental results, and elects to focus on some characteristic of selected planes, lines, and points in the domain.

The planar comparisons are not particularly strong for validation compared to quantitative comparison methods, but give a helpful picture of the general similarity between model and experiment. Figure 5 through Figure 9 in general show good agreement between the data and model contours. It is through these figures that a general concept of the flow is obtained. As the contaminant enters the domain, it is dispersed by bulk flow. The pollutant is swept vertically upward and against the lee-ward face of the tall building. The low wake velocities do not necessarily correlate to high concentrations downstream of the large structure, as the pollutant disperses with increasing height. The vertical velocity caused by the presence of the tall building appears to be the driving force for the significant vertical dispersion of the contaminant. The tall building acts as a barrier to the full stream flow and prevents the contaminant plume from being immediately swept downwind. The highest concentration is most notably present closest to the injection site and within the street canyon, closer to the tall building. The magnitude of subsequent decrease relates to the shielding effect of the surrounding buildings and apparent zones of low velocity. Velocity contours suggest a low velocity region in the direct wake of the building. This might be stagnation, but is more likely (as suggested by LES and TFNS point predictions) a region of high fluctuation.

Line plots more readily show the quantitative quality of the comparison between model and test data. Overall Figure 11 (a) shows excellent quantitative concentration match between LES/TFNS and experiment, despite the slight overestimation of velocity in this region. This overestimation of the velocity is apparent in both Figure 11 (b) and Figure 12. Figure 11 (b) shows an excellent match between experiment and LES and TFNS at 1/6H. However, at larger H, LES and TFNS appear to diverge from experimental behavior and show an increase in both velocity magnitude and y-direction velocity approaching the building immediately downwind. Inspection of the velocity components in Figure 12 shows a velocity mismatch occurs in the y-direction velocity component at 1/2H for LES and TFNS. Figure 14 shows the long-term downwind velocity behavior and demonstrates that LES/TFNS realigns with experimental results beyond the primary street canyon at 5/6H. At 1/2H, the LES velocity is lower than the data due to lower average velocity zones near the small buildings, while TFNS predictions are closer to the data. Despite these differences in velocity, Figure 14 (a) shows excellent contaminant dispersion modeling by LES and TFNS at 1/2H and 5/6H. Velocity values for the k-ε model are closer to the data than LES/TFNS in some cases. In Figure 11, there is little difference between the experimental velocity and the k- ε results at 1/2H and 5/6H. However, at 1/6H, the k-ε model exhibits a mismatch in the velocity magnitude primarily caused by differences

in the z-component (vertical) velocity. The k-ε model overestimates the concentration in every stream-wise comparison.

In the span-wise direction at the comparison points, LES and TFNS demonstrate concentration and velocity behavior close to the observed data. Figure 15 shows concentration and velocity magnitude data in the span-wise direction at varying height. Figure 15 (a) shows that the concentration is largely located at the center of the domain, closest to the injection site, and quickly approaches 0 away from the tall building. The LES confidence interval and TFNS models predict the expected concentration behavior well. At 1/2H, the LES and TFNS models slightly overestimate concentration level. The k-ε model overestimates the concentration at every height and the curve shapes resemble a simple distribution curve and doesn't mimic the more complex shape of the experimental curves. All numerical models match the observed velocity data, especially at 1/2H, and 5/6H. At 1/6H, the building wake flow is very obvious in the span-wise velocity predictions and data. The k-ε model exhibits the largest deviation from the experiment, mostly in the shape and magnitude of the peaks. At the center of the domain, the k-ε model underestimates the velocity magnitude by ~0.1 m/s and overestimates the velocity at the adjacent street intersections. LES and TFNS show a good match at this elevation. Inspection of the individual velocity components at each height shows that each numerical model matches the data well in all 3 components of velocity. At 1/6H, horizontal and vertical velocity components for numerical simulations match the data well and it is evident that deviations from the experiment are primarily in the z-direction (vertical). At higher elevations, the x and y velocity components are expected to be near zero because the bulk flow is primarily in the z-direction. At 1/2H, the x- and y-components of velocity are near zero except around the center of the domain, close to the tall building. The tall building draws the flow vertically upward and creates an area of low pressure, this results in lateral flows to fill the void (Heist et al. 2009). Near the top of the tallest building, all numerical components of velocity match the observed behavior well.

Figure 16 shows the velocity and concentration results along a vertical line. At the bottom of the channel, the experiment shows a concentration mixture fraction greater than 1, which is indicative of error and uncertainties in the data acquisition methods. LES and TFNS agree with the data well throughout, with the majority of the data points falling within the LES 95% confidence interval. The k-ε model overestimates the concentration in the vertical direction much as it did examining the lines in the other directions, but begins to approach observed behavior at heights larger than H. Figure 16 (b) shows that k-ε underestimates the velocity magnitude at elevations below 0.2 y/Y but matches experimental data quite well elsewhere. The experimental results indicate that the velocity field rapidly approaches free-stream flow above the roofline of the tall building (approximately 0.33 y/Y), however LES and TFNS begin approaching bulk flow velocity values at a slightly higher elevation. As LES and TFNS approach the bulk flow behavior, they also align with the experimental results.

In reference to the point analysis, the point data mean values are redundant to the figures. In fact, all prior figures contain the mean point data due to the coincidence of the points with the plane and line locations. The helpful additional information in the point data comes in the form of the standard deviations. The magnitudes of the

standard deviations for LES and TFNS are quite large relative to the means. This is suggestive of very turbulent flow. The TFNS and LES simulations suggest fairly high variability at these locations in the wake of the large structure. Velocity magnitudes are moderately different compared to those found in the data, and this represents the one of the more significant differences between the TFNS and LES model versus the data. This region where the comparisons are made also happens to be the wake area where the greatest variability is expected. Lacking data from the tests on the fluctuations, it is difficult to deduce what precisely is the reason for the difference. One possibility is that the MRV technique filters or averages the highest frequency data. The simulations also have a natural spatial and temporal filter that is based on mesh spacing and the timestep. The data will filter to the spatial resolution and to the data rate.

If a (fast) Fourier transform (FFT) is performed on the LES point simulation results, it can be seen that the lower 1/6H data have a higher relative contribution of the lower frequency, whereas the higher frequencies are relatively more important at higher elevations. This can be seen below in Figure 17. The lower elevations are where the data were better in line with the model, and also where the model predicts a more significant contribution of the lower frequency fluctuations based on generally higher magnitudes at frequencies below 10 Hz. This analysis could be suggestive of a filtering effect that might be present in the experiments or models that may be partially why the velocity data and models are different. Concentrations might be easier to match since they are subject to molecular diffusion, which might tend to reduce fluctuation intensity. Or it may be easier because concentration is more bounded (between 1 and 0) whereas velocity magnitude was not (0 to infinity). A different scenario with different characteristic frequency spectra might be instructive to evaluate in follow-on work. According to Elkins and Alley (2007), the MRV scan time is typically around a millisecond, only slightly longer than the numerical timesteps and high enough to capture intermediate frequencies. This may not be a factor in the discrepancy, but still an interesting observation regarding the flow predictions.

In the same regions, it is equally curious that the k-ε model velocity predictions closely match the experiments, while the data for concentration is appreciably below the model. This seems to be more easily understood based on the lack of fluctuation dynamics predicted by the RANS modeling. All transient lateral motion is modeled in the sub-grid, and the sub-grid model is inadequate for wake flow predictions of this nature. This is a known deficiency of RANS modeling, and suggests the need for higher fidelity models in highly turbulent wake regions. It is worth noting that between the RANS and LES predictions, the data are almost always within a reasonable proximity of a model prediction for all times and locations evaluated.

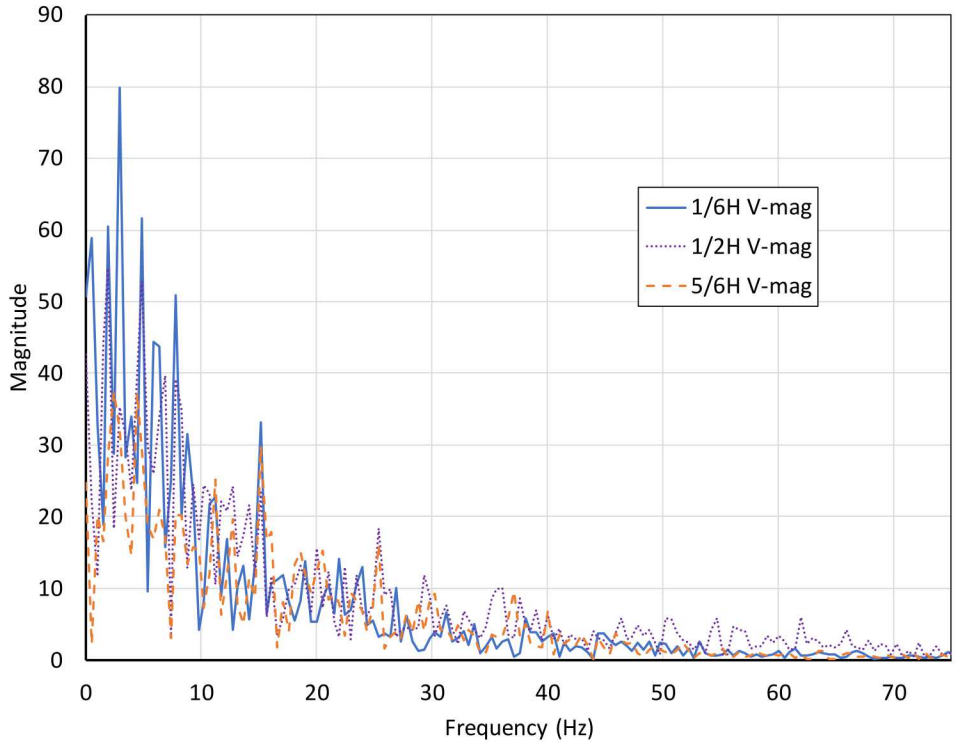

Figure 17. LES Velocity Magnitude Simulation Results Transposed into Frequency Domain via an FFT

This report does not show detailed differences between the LES parametric study, a deliberate omission. In the initial simulation review, LES results did not exhibit any obvious major outliers with the possible exception of the coarse model predictions. Instead of trying to parse the simulation results for what were apparently small scenario variations, we elected to represent the variation matrix as a range of model predictions. This range is a helpful representation for understanding model accuracies versus the data, but not helpful for specific parameter insight. A more detailed exploration of the individual parameters for this case is left to subsequent work.

All scenarios utilized wall functions, however there is varying validity of the wall function model due to the varying mesh scale and flow conditions. The baseline LES calculation had maximum y+ values just under 80 for the majority of the calculation. The coarse k-ε calculation had maximum y+ values around 90 for most of the calculation. For the coarse LES calculation it was around 80. For the fine LES calculation, the maximum y+ was typically around 50. The boundary layer model assumes y+ is in the log region between about 20-200 for ideal application. If this work were to be re-done, some slight mesh relaxation might be recommended approaching walls to have the maximum near the top end of the log region. The minimum y+ will always be difficult to capture for transient problems because localized stagnation can mean this approaches zero at some wall surfaces. Expanding the boundary layer in this case should capture more boundary flow in the ideal region. Shown in Figure 18 is the wall y+ for the k-ε model and the baseline LES model. This gives a better sense of where the flow resulted in outlier wall function boundary

simulations. Based on the legend color scheme, ideal boundary predictions involve yellow, green, and cyan. Red and violet boundaries are under-resolved, and blue and white are over-resolved. Except for what appears to be stagnation regions, the buildings have well resolved boundary layers. The ground is often over-resolved.

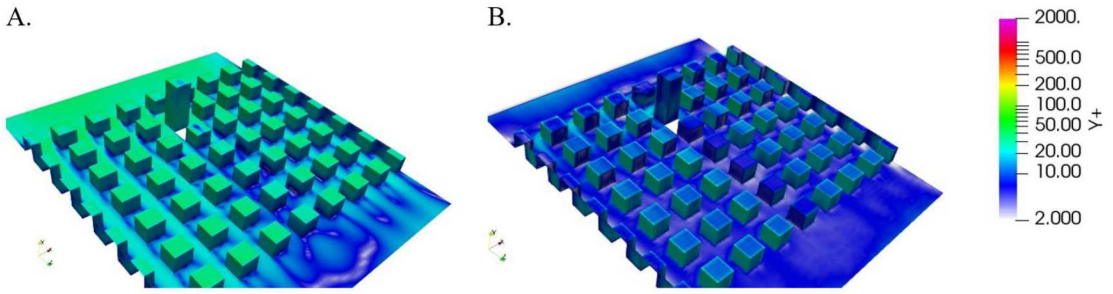

Figure 18. Graphical Illustration of Average (5-20 Seconds) y+ for k-ε (left) and Baseline LES (right)

The geometry for this scenario was symmetric, and one would anticipate symmetry in the resultant flows. However, the inflow boundary condition measured was not symmetric. This is believed to drive asymmetry in the results. A surprisingly good result is found in Figure 15 where the concentrations at 1/2H and 1/6H in the data show a bias to either side. The LES and TFNS models both predict the same trend, and magnitudes are fairly close to the data as well. This gives confidence in the simulation predictivity, but also highlights the importance of having the correct inflow conditions. Because everything else about the simulations was symmetric, the asymmetry in the results must be attributable to the inflow condition.

The inflow boundary condition was a point of difficulty with the initial simulation comparisons. The asymmetry in the wake was initially found to be surprisingly large in the models with coarser uniform meshes, which led to the non-uniform (biased) meshing and the inflow modeling method including the piecewise functional application of the flow condition and the parametric sensitivity focus on inflow conditions. The simulation results were informed by the test results, a luxury that may not be available for purely predictive exercises. The MRV technique did not provide more than an average at the boundary, and there is likely an effect of this assumption on the results. As an exercise to demonstrate that the mesh or solvers were not contributing to the asymmetry, the inflow boundary condition was mirrored, and the model predictions mirrored as well. The hope of the experimental team was that the up-wind structures would dominate the development of the wake flow and result in adequate comparisons downwind of the developed flow. While this may be mostly true, there is clearly an effect of the inflow condition on the resultant wake behavior that merits continuing attention to this feature.

This model versus data exercise is believed to be unique for CFD flow applications in that both the data and model produced an overwhelming amount of information. Comparison points, lines, and planes were selected as seemed reasonable to exhibit model and data behavior in regions of interest. Previously some note has been made regarding points of interest off center-plane. The data at varying x were only evaluated

directly between the tall building and the one immediately downstream. Some off-center comparison points may be instructive, but did not make the initial list of analysis comparisons. A more systematic way of identifying where to make comparisons may be helpful, but the technique for making this selection was not obvious at the time of the comparison.

This exercise illustrates a unique and detailed assessment of model accuracy by comparison to data in a relevant complex flow. It exposes problems not present in past comparisons because the data and model are in closer parity in terms of quantity and resolution of data than is normally obtained. Some methods require development that could benefit future comparisons of this nature. Some productive future work may include:

1. Consistent formats between simulation and experiment may enhance application of boundary conditions, as well as facilitate comparisons. For this exercise, the data were represented in Tecplot format, whereas SIERRA/Fuego used Exodus for output, and can read a 2D Exodus input file. While there are some utilities designed to facilitate data portability, this comparison proceeded before they could be modified and applied to this problem. Application of the boundary conditions could be simplified if it were appropriately formatted. Quantitative field comparisons might also be enabled in the future once this data issue is facilitated.

2. The validation comparison focused on specific points, lines, and planes. A much richer comparison is possible, but there needs to be thought given as to how to represent the comparison. We are not aware of methods that are mature for this type of comparison, and this represents an opportunity for validation and verification (V&V) technical development work provided existing data and simulation results exist. Tomographic reconstruction has been used in the past to probe jet flames, leveraging an axisymmetric assumption in the data (e.g. Meier et al., 2000). Full 3-D datasets and corresponding comparisons are not found in the atmospheric dispersion literature, nor have they been found elsewhere.

3. Validation is a philosophical endeavor, and quantification of accuracy lends to an enhancement in modeling utility. There are opportunities with this and like datasets to augment the utility of CFD if ways can be found to leverage the richness of the output from both exercises to make quantitative assertions about the accuracy of the models.

4. Tighter interactions between the experimental and modeling teams would have benefits to the activity. Testing occurred without pre-test simulations, which may have been instructive in defining open experimental parameters like the flow velocity and the geometry. The test team benefits the modeling team with improved representation of the data accuracies including the boundary conditions, experimental aleatory uncertainty, and guidance on the resolution thresholds.

5. At some point it will be helpful to more tightly establish the basis for use of water flows as surrogate for atmospheric air flows and dispersion using these techniques. While the techniques of scaling by self-similarity assumptions is relatively mature in engineering practice, such an activity can help augment the basis and uncover the limitations of such assumptions so that they can be used with increasing confidence in the future.

6. There are a myriad of alternate geometries and conditions of significant interest that can benefit from this type of analysis. Extending the data collection to thermal problems that might include density gradients and natural or forced convection can have broad impact to a lot of engineering design and test problems.

7. Atmospheric dispersion is normally assumed to be partly governed by the boundary layer scales as described in more detail in the introduction. With this scenario, the boundary layer was what was obtained from the test, and may not be representative of a specific urban flow environment. Developing application relevant inflow conditions would need to be accomplished before deploying the test capability as a scale model for practical atmospheric urban dispersion conditions.

8. The inflow conditions were lacking temporal information, and the mean velocity field may be inadequate to fully describe the inlet conditions. Some notion of the variability at the inflow plane would be helpful. Characterization of internal fluctuations might be helpful as well, but are not as critical to the accurate definition of the CFD model.

5. CONCLUSIONS

A series of computational simulations has been performed for dispersion of a contaminant in a geometry inspired by atmospheric conditions of interest. The simulations are compared with 3-D water channel flow measurements using the MRV/MRC technique. A parameter study involving turbulence models as well as a variety of convergence and parametric variations is used to assess model uncertainty. The models and experiments compare quite well, with the data being in the proximity of simulation predictions for all comparisons. Some models exhibited localized deviation from the data, with the wake region immediately downstream of the large building being the region of most significant difficulty. The MRV dataset represents an unusually detailed opportunity to assess model and experimental uncertainty for a problem of practical interest. Additional V&V methods work is needed to derive quantitative accuracy information for this type of flow.

REFERENCES

Addepalli, B. and Pardyjak, E.R., 2015. A study of flow fields in step-down street canyons. *Environmental Fluid Mechanics*, *15*(2), pp.439-481.

Benson, M.J., Elkins, C.J. and Eaton, J.K., 2011. Measurements of 3D velocity and scalar field for a film-cooled airfoil trailing edge. *Experiments in fluids*, *51*(2), pp.443-455.

Brixey, L.A., Heist, D.K., Richmond-Bryant, J., Bowker, G.E., Perry, S.G. and Wiener, R.W., 2009. The effect of a tall tower on flow and dispersion through a model urban neighborhood Part 2. Pollutant dispersion. *Journal of Environmental Monitoring*, *11*(12), pp.2171-2179.

Brown, A.L. and Dabberdt, W.F., 2003. Modeling ventilation and dispersion for covered roadways. *Journal of Wind Engineering and Industrial Aerodynamics*, *91*(5), pp.593-608.

Chang, S., Elkins, C., Alley, M., Eaton, J. and Monismitha, S., 2009. Flow inside a coral colony measured using magnetic resonance velocimetry. *Limnology and Oceanography*, *54*(5), pp.1819-1827.

Elkins, C.J. and Alley, M.T., 2007. Magnetic resonance velocimetry: applications of magnetic resonance imaging in the measurement of fluid motion. *Experiments in Fluids*, 43(6), pp.823-858.

Elkins, C.J., Alley, M.T., Saetran, L. and Eaton, J.K., 2009. Three-dimensional magnetic resonance velocimetry measurements of turbulence quantities in complex flow. *Experiments in Fluids*, 46(2), pp.285-296.

Elkins, C.J., Markl, M., Iyengar, A., Wicker, R. and Eaton, J.K., 2004. Full-field velocity and temperature measurements using magnetic resonance imaging in turbulent complex internal flows. International *journal of heat and fluid flow*, 25(5), pp.702-710.

Elkins, C.J., Markl, M., Pelc, N. and Eaton, J.K., 2003. 4D Magnetic resonance velocimetry for mean velocity measurements in complex turbulent flows. *Experiments in Fluids*, 34(4), pp.494-503.

Franzese, P. and Huq, P., 2011. Urban dispersion modelling and experiments in the daytime and nighttime atmosphere. *Boundary-layer meteorology*, *139*(3), pp.395-409.

Hayati, A.N., Stoll, R., Kim, J.J., Harman, T., Nelson, M.A., Brown, M.J. and Pardyjak, E.R., 2017. Comprehensive Evaluation of Fast-Response, Reynolds-Averaged Navier–Stokes, and Large-Eddy Simulation Methods Against High-Spatial-Resolution Wind-Tunnel Data in Step-Down Street Canyons. *Boundary-Layer Meteorology*, *164*(2), pp.217-247.

Heist, D.K., Brixey, L.A., Richmond-Bryant, J., Bowker, G.E., Perry, S.G. and Wiener, R.W., 2009. The effect of a tall tower on flow and dispersion through a model urban neighborhood Part 1. Flow characteristics. *Journal of Environmental Monitoring*, *11*(12), pp.2163-2170.

Jones, W.P. and Launder, B., 1972. The prediction of laminarization with a two-equation model of turbulence. *International journal of heat and mass transfer*, *15*(2), pp.301-314.

Kim, W.W., Menon, S., Kim, W.W. and Menon, S., 1997, January. Application of the localized dynamic subgrid-scale model to turbulent wall-bounded flows. In *35th aerospace sciences meeting and exhibit* (p. 210).

Laskowski, G.M., Kearney, S.P., Evans, G. and Greif, R., 2007. Mixed convection heat transfer to and from a horizontal cylinder in cross-flow with heating from below. *International journal of heat and fluid flow*, *28*(3), pp.454-468

Lateb, M., Meroney, R.N., Yataghene, M., Fellouah, H., Saleh, F. and Boufadel, M.C., 2016. On the use of numerical modelling for near-field pollutant dispersion in urban environments− A review. *Environmental Pollution*, *208*, pp.271-283.

Launder, B.E. and Spalding, D.B., 1983. The numerical computation of turbulent flows. In *Numerical Prediction of Flow, Heat Transfer, Turbulence and Combustion* (pp. 96-116).

Meier, W., Barlow, R.S., Chen, Y.L. and Chen, J.Y., 2000. Raman/Rayleigh/LIF measurements in a turbulent CH4/H2/N2 jet diffusion flame: experimental techniques and turbulence–chemistry interaction. Combustion and Flame, 123(3), pp.326-343.

Pascheke, F., Barlow, J.F. and Robins, A., 2008. Wind-tunnel modelling of dispersion from a scalar area source in urban-like roughness. *Boundary-Layer Meteorology*, *126*(1), pp.103-124.

Saathoff, P., Gupta, A., Stathopoulos, T. and Lazure, L., 2009. Contamination of fresh air intakes due to downwash from a rooftop structure. *Journal of the Air & Waste Management Association*, *59*(3), pp.343-353.

Shen, J., Gao, Z., Ding, W. and Yu, Y., 2017. An investigation on the effect of street morphology to ambient air quality using six real-world cases. *Atmospheric Environment*, *164*, pp.85-101.

Sierra Thermal Fluids Development Team, "Sierra Low Mach Module: Fuego Theory Manual – Version 4.44," Sandia National Laboratories, SAND 2017-3774, (2017a).

Sierra Thermal Fluids Development Team, "Sierra Low Mach Module: Fuego User Manual – Version 4.44," Sandia National Laboratories, SAND 2017-3792, (2017b).

Tieszen, S.R., Domino, S.P. and Black, A.R., 2005. *Validation of a simple turbulence model suitable for closure of temporally-filtered Navier-Stokes equations using a helium plume* (No. SAND2005-3210). Sandia National Laboratories.

Van Leer, B., 1979. Towards the ultimate conservative difference scheme. V. A second-order sequel to Godunov's method. *Journal of computational Physics*, *32*(1), pp.101-136.

Xie, Z.T., Coceal, O. and Castro, I.P., 2008. Large-eddy simulation of flows over random urban-like obstacles. *Boundary-layer meteorology*, *129*(1), p.1.

APPENDIX A: THE BASELINE LES INPUT FILE

```
# <Problem_Description>
#
# Flow around a building array
# 3D, time-dependent
# LES turbulence model
#
# </Problem_Description>

Begin Sierra Fuego

  Title Flow Around Building Array


$-------------------------------------------------
$  Define material properties to be used
$-------------------------------------------------
  Begin Property Specification For Fuego Material Water
    Specific_heat           = 4.18e07
    Reference Temperature       = 294.15 $k
    density              = 997.97    $ kg/m^3
    viscosity             = 0.00098    $ Pa*s
    REFERENCE mixture_fraction    = 0.0
    SCHMIDT_NUMBER          = 0.9
    PRANDTL_NUMBER          = 0.9

  End  Property Specification For Fuego Material Water

$-------------------------------------------------
$  Define global constants
$-------------------------------------------------

 Begin Global Constants turb
  Turbulence Model Prandtl Number = 0.9
  Turbulence Model Schmidt Number = 0.9
  GRAVITY VECTOR = 0.0, -9.80665, 0 #mks units
 END  Global Constants turb

$-------------------------------------------------
$  Define velocity functions
$-------------------------------------------------

  begin definition for function inlet_vel01
   type is Piecewise Linear
   begin values

$    0.0   0.0
    0.0098 0.1232
    0.0196 0.1751
    0.0294 0.1975
    0.0392 0.2121
    0.0490 0.2231
    0.0588 0.2131
    0.0686 0.2090
    0.0784 0.1855
    0.0882 0.1772
    0.0980 0.1691
    0.1078 0.1790
    0.1176 0.1646
    0.1274 0.1721
    0.1372 0.1997
    0.1470 0.1810
```

```
    0.1568 0.1813
    0.1666 0.1684
    0.1764 0.1246
    0.1862 0.0803
$    0.196  0.0

  end values
  end definition for function inlet_vel01

begin definition for function inlet_vel02
   type is Piecewise Linear
   begin values

$    0.0   0.0
    0.0098 0.1797
    0.0196 0.2310
    0.0294 0.2635
    0.0392 0.2802
    0.0490 0.2762
    0.0588 0.2735
    0.0686 0.2692
    0.0784 0.2543
    0.0882 0.2345
    0.0980 0.2318
    0.1078 0.2344
    0.1176 0.2280
    0.1274 0.2440
    0.1372 0.2716
    0.1470 0.2669
    0.1568 0.2672
    0.1666 0.2436
    0.1764 0.2097
    0.1862 0.1578
$    0.196  0.0


 end values
  end definition for function inlet_vel02

begin definition for function inlet_vel03
   type is Piecewise Linear
   begin values
$    0.0   0.0
    0.0098 0.2182
    0.0196 0.2698
    0.0294 0.2948
    0.0392 0.3102
    0.0490 0.3146
    0.0588 0.3146
    0.0686 0.3155
    0.0784 0.2985
    0.0882 0.2798
    0.0980 0.2706
    0.1078 0.2741
    0.1176 0.2642
    0.1274 0.2942
    0.1372 0.3117
    0.1470 0.3125
    0.1568 0.3073
    0.1666 0.2890
    0.1764 0.2542
    0.1862 0.2004
$    0.196  0.0
```

```
 end values
  end definition for function inlet_vel03

begin definition for function inlet_vel04
   type is Piecewise Linear
   begin values
$    0.0   0.0
    0.0098 0.2398
    0.0196 0.2993
    0.0294 0.3132
    0.0392 0.3201
    0.0490 0.3279
    0.0588 0.3276
    0.0686 0.3249
    0.0784 0.3080
    0.0882 0.2947
    0.0980 0.2870
    0.1078 0.2892
    0.1176 0.2914
    0.1274 0.3128
    0.1372 0.3289
    0.1470 0.3280
    0.1568 0.3220
    0.1666 0.3005
    0.1764 0.2637
    0.1862 0.2211
$    0.196  0.0

 end values
  end definition for function inlet_vel04

begin definition for function inlet_vel05
   type is Piecewise Linear
   begin values
$    0.0   0.0
    0.0098 0.2544
    0.0196 0.3116
    0.0294 0.3288
    0.0392 0.3359
    0.0490 0.3420
    0.0588 0.3424
    0.0686 0.3305
    0.0784 0.3118
    0.0882 0.3082
    0.0980 0.3043
    0.1078 0.3014
    0.1176 0.3107
    0.1274 0.3213
    0.1372 0.3374
    0.1470 0.3488
    0.1568 0.3319
    0.1666 0.2975
    0.1764 0.2620
    0.1862 0.2213
$    0.196  0.0

 end values
  end definition for function inlet_vel05

begin definition for function inlet_vel06
   type is Piecewise Linear
   begin values
```

```
$    0.0   0.0
    0.0098 0.2619
    0.0196 0.3129
    0.0294 0.3254
    0.0392 0.3343
    0.0490 0.3613
    0.0588 0.3514
    0.0686 0.3398
    0.0784 0.3161
    0.0882 0.3230
    0.0980 0.3229
    0.1078 0.3246
    0.1176 0.3230
    0.1274 0.3329
    0.1372 0.3494
    0.1470 0.3648
    0.1568 0.3372
    0.1666 0.2993
    0.1764 0.2696
    0.1862 0.2356
$    0.196  0.0

 end values
  end definition for function inlet_vel06

begin definition for function inlet_vel07
   type is Piecewise Linear
   begin values
$    0.0   0.0
    0.0098 0.2631
    0.0196 0.3123
    0.0294 0.3240
    0.0392 0.3423
    0.0490 0.3608
    0.0588 0.3604
    0.0686 0.3432
    0.0784 0.3348
    0.0882 0.3356
    0.0980 0.3448
    0.1078 0.3391
    0.1176 0.3411
    0.1274 0.3398
    0.1372 0.3645
    0.1470 0.3711
    0.1568 0.3397
    0.1666 0.3002
    0.1764 0.2742
    0.1862 0.2340
$    0.196  0.0

 end values
  end definition for function inlet_vel07

begin definition for function inlet_vel08
   type is Piecewise Linear
   begin values
$    0.0   0.0
    0.0098 0.2631
    0.0196 0.3123
    0.0294 0.3240
    0.0392 0.3423
    0.0490 0.3608
    0.0588 0.3604
```

```
    0.0686 0.3432
    0.0784 0.3348
    0.0882 0.3356
    0.0980 0.3448
    0.1078 0.3391
    0.1176 0.3411
    0.1274 0.3398
    0.1372 0.3645
    0.1470 0.3711
    0.1568 0.3397
    0.1666 0.3002
    0.1764 0.2742
    0.1862 0.2340
$    0.196  0.0

 end values
  end definition for function inlet_vel08

begin definition for function inlet_vel09
   type is Piecewise Linear
   begin values
$    0.0   0.0
    0.0098 0.2744
    0.0196 0.2967
    0.0294 0.3143
    0.0392 0.3506
    0.0490 0.3725
    0.0588 0.3808
    0.0686 0.3699
    0.0784 0.3582
    0.0882 0.3772
    0.0980 0.3793
    0.1078 0.3753
    0.1176 0.3575
    0.1274 0.3670
    0.1372 0.3918
    0.1470 0.3800
    0.1568 0.3392
    0.1666 0.3086
    0.1764 0.2793
    0.1862 0.2441
$    0.196  0.0

 end values
  end definition for function inlet_vel09

begin definition for function inlet_vel10
   type is Piecewise Linear
   begin values
$    0.0   0.0
    0.0098 0.2758
    0.0196 0.2911
    0.0294 0.3117
    0.0392 0.3444
    0.0490 0.3705
    0.0588 0.3814
    0.0686 0.3795
    0.0784 0.3719
    0.0882 0.3943
    0.0980 0.4011
    0.1078 0.3867
    0.1176 0.3665
    0.1274 0.3780
```

```
    0.1372 0.4007
    0.1470 0.3759
    0.1568 0.3367
    0.1666 0.3110
    0.1764 0.2814
    0.1862 0.2492
$    0.196  0.0

 end values
  end definition for function inlet_vel10

begin definition for function inlet_vel11
   type is Piecewise Linear
   begin values

$    0.0   0.0
    0.0098 0.2757
    0.0196 0.2763
    0.0294 0.3054
    0.0392 0.3297
    0.0490 0.3643
    0.0588 0.3920
    0.0686 0.3878
    0.0784 0.3823
    0.0882 0.4050
    0.0980 0.4158
    0.1078 0.3993
    0.1176 0.3769
    0.1274 0.3814
    0.1372 0.4019
    0.1470 0.3718
    0.1568 0.3282
    0.1666 0.3048
    0.1764 0.2718
    0.1862 0.2488
$    0.196  0.0

 end values
  end definition for function inlet_vel11

begin definition for function inlet_vel12
   type is Piecewise Linear
   begin values

$    0.0   0.0
    0.0098 0.2687
    0.0196 0.2713
    0.0294 0.2936
    0.0392 0.3227
    0.0490 0.3625
    0.0588 0.3941
    0.0686 0.3936
    0.0784 0.3918
    0.0882 0.4217
    0.0980 0.4351
    0.1078 0.4059
    0.1176 0.3874
    0.1274 0.4003
    0.1372 0.4087
    0.1470 0.3588
    0.1568 0.3259
    0.1666 0.3042
    0.1764 0.2566
```

```
    0.1862 0.2488
$    0.196  0.0

 end values
  end definition for function inlet_vel12

begin definition for function inlet_vel13
   type is Piecewise Linear
   begin values

$    0.0   0.0
    0.0098 0.2547
    0.0196 0.2631
    0.0294 0.2823
    0.0392 0.3268
    0.0490 0.3556
    0.0588 0.3945
    0.0686 0.4021
    0.0784 0.3954
    0.0882 0.4329
    0.0980 0.4438
    0.1078 0.4200
    0.1176 0.4045
    0.1274 0.4154
    0.1372 0.4100
    0.1470 0.3771
    0.1568 0.3297
    0.1666 0.3025
    0.1764 0.2596
    0.1862 0.2392
$    0.196  0.0

 end values
  end definition for function inlet_vel13

begin definition for function inlet_vel14
   type is Piecewise Linear
   begin values

$    0.0   0.0
    0.0098 0.2399
    0.0196 0.2580
    0.0294 0.2910
    0.0392 0.3234
    0.0490 0.3583
    0.0588 0.3920
    0.0686 0.4024
    0.0784 0.4082
    0.0882 0.4420
    0.0980 0.4537
    0.1078 0.4328
    0.1176 0.4137
    0.1274 0.4212
    0.1372 0.4133
    0.1470 0.3747
    0.1568 0.3351
    0.1666 0.3012
    0.1764 0.2586
    0.1862 0.2335
$    0.196  0.0

 end values
  end definition for function inlet_vel14
```

```
begin definition for function inlet_vel15
   type is Piecewise Linear
   begin values

$    0.0   0.0
     0.0098 0.2349
     0.0196 0.2601
     0.0294 0.2835
     0.0392 0.3249
     0.0490 0.3608
     0.0588 0.3883
     0.0686 0.4098
     0.0784 0.4150
     0.0882 0.4383
     0.0980 0.4554
     0.1078 0.4371
     0.1176 0.4115
     0.1274 0.4206
     0.1372 0.4116
     0.1470 0.3703
     0.1568 0.3308
     0.1666 0.3073
     0.1764 0.2660
     0.1862 0.2286
$    0.196  0.0

 end values
  end definition for function inlet_vel15

begin definition for function inlet_vel16
   type is Piecewise Linear
   begin values

$    0.0   0.0
     0.0098 0.2488
     0.0196 0.2788
     0.0294 0.2976
     0.0392 0.3238
     0.0490 0.3632
     0.0588 0.3935
     0.0686 0.4140
     0.0784 0.4151
     0.0882 0.4303
     0.0980 0.4408
     0.1078 0.4327
     0.1176 0.4137
     0.1274 0.4228
     0.1372 0.4139
     0.1470 0.3759
     0.1568 0.3323
     0.1666 0.3077
     0.1764 0.2771
     0.1862 0.2375
$    0.196  0.0

 end values
  end definition for function inlet_vel16

begin definition for function inlet_vel17
   type is Piecewise Linear
   begin values
```

```
$    0.0   0.0
    0.0098 0.2790
    0.0196 0.3055
    0.0294 0.3096
    0.0392 0.3339
    0.0490 0.3650
    0.0588 0.3922
    0.0686 0.4081
    0.0784 0.4077
    0.0882 0.4180
    0.0980 0.4288
    0.1078 0.4268
    0.1176 0.3973
    0.1274 0.4111
    0.1372 0.4089
    0.1470 0.3812
    0.1568 0.3409
    0.1666 0.3114
    0.1764 0.2937
    0.1862 0.2493
$    0.196  0.0

 end values
  end definition for function inlet_vel17

begin definition for function inlet_vel18
   type is Piecewise Linear
   begin values

$    0.0   0.0
    0.0098 0.2990
    0.0196 0.3206
    0.0294 0.3237
    0.0392 0.3416
    0.0490 0.3623
    0.0588 0.3802
    0.0686 0.3826
    0.0784 0.3843
    0.0882 0.3913
    0.0980 0.4053
    0.1078 0.4045
    0.1176 0.3774
    0.1274 0.3825
    0.1372 0.3935
    0.1470 0.3750
    0.1568 0.3467
    0.1666 0.3192
    0.1764 0.3047
    0.1862 0.2693
$    0.196  0.0

 end values
  end definition for function inlet_vel18

begin definition for function inlet_vel19
   type is Piecewise Linear
   begin values

$    0.0   0.0
    0.0098 0.2955
    0.0196 0.3282
    0.0294 0.3340
    0.0392 0.3457
```

```
    0.0490 0.3532
    0.0588 0.3659
    0.0686 0.3552
    0.0784 0.3537
    0.0882 0.3666
    0.0980 0.3774
    0.1078 0.3824
    0.1176 0.3515
    0.1274 0.3577
    0.1372 0.3685
    0.1470 0.3496
    0.1568 0.3326
    0.1666 0.3267
    0.1764 0.3006
    0.1862 0.2593
$    0.196  0.0

 end values
  end definition for function inlet_vel19

begin definition for function inlet_vel20
   type is Piecewise Linear
   begin values

$    0.0   0.0
    0.0098 0.2084
    0.0196 0.2378
    0.0294 0.2472
    0.0392 0.2464
    0.0490 0.2539
    0.0588 0.2601
    0.0686 0.2530
    0.0784 0.2514
    0.0882 0.2610
    0.0980 0.2645
    0.1078 0.2736
    0.1176 0.2480
    0.1274 0.2499
    0.1372 0.2579
    0.1470 0.2471
    0.1568 0.2399
    0.1666 0.2345
    0.1764 0.2173
    0.1862 0.1944
$    0.196  0.0

 end values
  end definition for function inlet_vel20


$ BEGIN DEFINITION FOR FUNCTION gasVolFcn
$  TYPE IS PIECEWISE LINEAR
$  BEGIN VALUES
$
$     0.0  1.0
$     0.228 1.0
$     0.238 0.8
$     0.24 0.8
$
$  END VALUES
$ END DEFINITION FOR FUNCTION gasVolFcn
```

```
$-----------------------------------------------
$  Define linear solver settings
$-----------------------------------------------
  Begin Trilinos Equation Solver Continuity
    Solution Method = GMRES
    Preconditioning Method = Multilevel
    Restart Iterations = 100
    Maximum Iterations = 100
    Residual Norm Tolerance = 1.0e-5
    Residual Norm Scaling = R0
  End  Trilinos Equation Solver Continuity

  Begin Aztec Equation Solver Scalar
    Solution Method = GMRES
    Preconditioning Method = Symmetric-gauss-seidel
    Preconditioning Steps = 1
    Restart Iterations = 50
    Maximum Iterations = 50
    Residual Norm Tolerance = 1.0e-4
    Residual Norm Scaling = R0
  End  Aztec Equation Solver Scalar

$-----------------------------------------------
$  Specify mesh name and settings
$-----------------------------------------------
  Begin Finite Element Model Water_flow
    Database Name = ../meshes/Medium_02.g
    Database Type = ExodusII

$-----------------------------------------------
$    Assign material properties to element blocks
$-----------------------------------------------
    Begin Parameters For Block block_1
      Material Water
    End  Parameters For Block block_1
  End  Finite Element Model Water_flow

$ RESTART = automatic

$-------------------------------------------------------
$  Procedure domain - solution control, region settings
$-------------------------------------------------------

  Begin Fuego Procedure Fuego_procedure

$-----------------------------------------------
$    Define temporal solution parameters
$-----------------------------------------------
    Time Start = 0.0, Stop = 20.0, Status Interval = 10

    Begin Solution Control Description
      Use System Main

      begin initialize mytransient_init
         advance Fuego_region
      end  initialize mytransient_init

      Begin System Main
         use initialize mytransient_init

        Begin transient mytransient
          Advance Fuego_region
        End  transient mytransient
```

```
      End  System Main

$-------------------------------------------------
$      Define time integration parameters
$-------------------------------------------------
      Begin Parameters For transient mytransient
        Start Time = 0.0
        Initial Deltat = 0.0005
$        Initial Deltat = 1.5e-3
        Termination Time Is 20.0

$        Begin Parameters for Fuego Region Fuego_region
$          Transient Step Type is Automatic
$         CFL Limit = 1.0
$          Time Step Change Factor = 1.5
$        End  Parameters for Fuego Region Fuego_region
      End  Parameters For transient mytransient

    End  Solution Control Description

$-------------------------------------------------
$    Region domain - EQs, BCs, ICs, post-processing
$-------------------------------------------------

    Begin Fuego Region Fuego_region

$-------------------------------------------------
$  Define Unit Conversions
$-------------------------------------------------
    SET LENGTH UNIT CONVERSION FACTOR = 100.0 $ meters rather than cm
    SET MASS  UNIT CONVERSION FACTOR = 1000.0 $ kg rather than g
    SET TIME  UNIT CONVERSION FACTOR = 1.0  $ seconds - keep
    SET TEMPERATURE UNITS = Kelvin       $ Default

$-----------------------------------------------------
$      Specify solution steering options
$-----------------------------------------------------
      Use Solution Steering With Interval = 4

$-----------------------------------------------------
$      Solution options - equations, solver options
$-----------------------------------------------------
      Begin Solution Options

$-------------------------------------------------
$        Specify coordinate system
$-------------------------------------------------
        Coordinate System = 3D

$-------------------------------------------------
$        Specify equations to solve
$-------------------------------------------------
        Activate Equation Continuity
        Activate Equation X_momentum
        Activate Equation Y_momentum
        Activate Equation Z_momentum
        Activate Equation Mixture_Fraction
        Activate Equation Turbulent_Kinetic_Energy

        Use Equation Solver Continuity For Equation Continuity
        Use Equation Solver Scalar   For Equation X_momentum
        Use Equation Solver Scalar   For Equation Y_momentum
```

```
        Use Equation Solver Scalar   For Equation Z_momentum
        Use Equation Solver Scalar   For Equation Mixture_Fraction
        Use Equation Solver Scalar   For Equation Turbulent_Kinetic_Energy

$-------------------------------------------------
$        Define nonlinear solver parameters
$-------------------------------------------------
        Minimum Number Of Nonlinear Iterations = 1
        Maximum Number Of Nonlinear Iterations = 1

$-------------------------------------------------
$        Specify pressure smoothing
$-------------------------------------------------
        Projection Method = Fourth_order Smoothing With Timestep Scaling

$-------------------------------------------------
$        Specify upwinding parameters
$-------------------------------------------------
        Upwind Method Is Upw  For Equation X_momentum
        Upwind Method Is Upw  For Equation Y_momentum
        Upwind Method Is Upw  For Equation Z_momentum
        Upwind Method Is Upw  For Equation Mixture_Fraction
        Upwind Method Is Upw  For Equation Turbulent_Kinetic_Energy

        First Order Upwind Factor = 0.0 For Equation X_momentum
        First Order Upwind Factor = 0.0 For Equation Y_momentum
        First Order Upwind Factor = 0.0 For Equation Z_momentum
        First Order Upwind Factor = 0.0 For Equation Mixture_Fraction
        First Order Upwind Factor = 0.0 For Equation Turbulent_Kinetic_Energy

        Hybrid Upwind Factor = 0.0 For Equation X_momentum
        Hybrid Upwind Factor = 0.0 For Equation Y_momentum
        Hybrid Upwind Factor = 0.0 For Equation Z_momentum
        Hybrid Upwind Factor = 0.1 For Equation Mixture_Fraction
        Hybrid Upwind Factor = 0.1 For Equation Turbulent_Kinetic_Energy

$-------------------------------------------------
$        Specify under-relaxation
$-------------------------------------------------
        Under Relax Momentum By 1.0
        Under Relax Pressure By 1.0
        Under Relax Turbulent_Kinetic_Energy by 1.0

$-------------------------------------------------
$        Define turbulence model
$-------------------------------------------------
        Begin Turbulence Model Specification
$          Turbulence Model = Dsmag
$          Under Relax Turbulent_viscosity By 0.7

           Turbulence Model = Ksgs
           Under Relax Turbulent_viscosity By 0.75
           Include Molecular Viscosity In K-E Diffusion Coefficient


        End  Turbulence Model Specification

$-------------------------------------------------
$        Define buoyancy model
$-------------------------------------------------
$        Begin Buoyancy Model Specification Bouyant
$          Buoyancy Reference Temperature = 294.15
$          Buoyancy Model = Differential
```

```
$        End  Buoyancy Model Specification

$-------------------------------------------------
$        Define darcy flow
$-------------------------------------------------

$     # specify properties for the solid phase
$     BEGIN MULTIPHASE MODEL SPECIFICATION myMult
$      # turn on model for porous media (Darcy flow)
$      ENABLE POROUS MEDIA MODEL
$      multiphase particle_diameter = 0.005
$      multiphase solid_velocity = 0.0
$     END MULTIPHASE MODEL SPECIFICATION myMult

      End  Solution Options

$-----------------------------------------------------------
$      Specify which mesh model to use for this region
$-----------------------------------------------------------
      Use Finite Element Model Water_flow

$-------------------------------------------------
$      Specify initial conditions
$-------------------------------------------------
      Begin Initial Condition Block IC_block
        Volume Is block_1
        Pressure = 0.0
        X_velocity = 0.0
        Y_velocity = 0.0
        Z_velocity = 0.0
        Temperature = 294.15
        Mixture_Fraction = 0.0
        Turbulent_Kinetic_Energy = 1e-6
$        function for gas_volume_fraction = gasVolFcn IN THE Z DIRECTION
      End  Initial Condition Block IC_block

$-------------------------------------------------
$      Define boundary conditions
$-------------------------------------------------
      # Inflow
      Begin Inflow Boundary Condition On Surface surface_1
        X_velocity = 0.0
        Y_velocity = 0.0
$        Z_velocity = .323 $ avg from inlet data
        function for Z_velocity = inlet_vel01 IN THE X DIRECTION
        Temperature = 294.15
        Mixture_Fraction = 0.0
        Turbulent_Kinetic_Energy = 1.0e-6

      End  Inflow Boundary Condition On Surface surface_1

      # Inflow
      Begin Inflow Boundary Condition On Surface surface_2
        X_velocity = 0.0
        Y_velocity = 0.0
$        Z_velocity = .323 $ avg from inlet data
        function for Z_velocity = inlet_vel02 IN THE X DIRECTION
        Temperature = 294.15
        Mixture_Fraction = 0.0
        Turbulent_Kinetic_Energy = 1.0e-6

      End  Inflow Boundary Condition On Surface surface_2
```

```
      # Inflow
      Begin Inflow Boundary Condition On Surface surface_3
        X_velocity = 0.0
        Y_velocity = 0.0
$        Z_velocity = .323 $ avg from inlet data
        function for Z_velocity = inlet_vel03 IN THE X DIRECTION
        Temperature = 294.15
        Mixture_Fraction = 0.0
        Turbulent_Kinetic_Energy = 1.0e-6

      End  Inflow Boundary Condition On Surface surface_3

      # Inflow
      Begin Inflow Boundary Condition On Surface surface_4
        X_velocity = 0.0
        Y_velocity = 0.0
$        Z_velocity = .323 $ avg from inlet data
        function for Z_velocity = inlet_vel04 IN THE X DIRECTION
        Temperature = 294.15
        Mixture_Fraction = 0.0
        Turbulent_Kinetic_Energy = 1.0e-6

      End  Inflow Boundary Condition On Surface surface_4

      # Inflow
      Begin Inflow Boundary Condition On Surface surface_5
        X_velocity = 0.0
        Y_velocity = 0.0
$        Z_velocity = .323 $ avg from inlet data
        function for Z_velocity = inlet_vel05 IN THE X DIRECTION
        Temperature = 294.15
        Mixture_Fraction = 0.0
        Turbulent_Kinetic_Energy = 1.0e-6

      End  Inflow Boundary Condition On Surface surface_5

      # Inflow
      Begin Inflow Boundary Condition On Surface surface_6
        X_velocity = 0.0
        Y_velocity = 0.0
$        Z_velocity = .323 $ avg from inlet data
        function for Z_velocity = inlet_vel06 IN THE X DIRECTION
        Temperature = 294.15
        Mixture_Fraction = 0.0
        Turbulent_Kinetic_Energy = 1.0e-6

      End  Inflow Boundary Condition On Surface surface_6

      # Inflow
      Begin Inflow Boundary Condition On Surface surface_7
        X_velocity = 0.0
        Y_velocity = 0.0
$        Z_velocity = .323 $ avg from inlet data
        function for Z_velocity = inlet_vel07 IN THE X DIRECTION
        Temperature = 294.15
        Mixture_Fraction = 0.0
        Turbulent_Kinetic_Energy = 1.0e-6

      End  Inflow Boundary Condition On Surface surface_7

      # Inflow
      Begin Inflow Boundary Condition On Surface surface_8
```

```
        X_velocity = 0.0
        Y_velocity = 0.0
$        Z_velocity = .323 $ avg from inlet data
        function for Z_velocity = inlet_vel08 IN THE X DIRECTION
        Temperature = 294.15
        Mixture_Fraction = 0.0
        Turbulent_Kinetic_Energy = 1.0e-6

      End  Inflow Boundary Condition On Surface surface_8

      # Inflow
      Begin Inflow Boundary Condition On Surface surface_9
        X_velocity = 0.0
        Y_velocity = 0.0
$        Z_velocity = .323 $ avg from inlet data
        function for Z_velocity = inlet_vel09 IN THE X DIRECTION
        Temperature = 294.15
        Mixture_Fraction = 0.0
        Turbulent_Kinetic_Energy = 1.0e-6

      End  Inflow Boundary Condition On Surface surface_9

      # Inflow
      Begin Inflow Boundary Condition On Surface surface_10
        X_velocity = 0.0
        Y_velocity = 0.0
$        Z_velocity = .323 $ avg from inlet data
        function for Z_velocity = inlet_vel10 IN THE X DIRECTION
        Temperature = 294.15
        Mixture_Fraction = 0.0
        Turbulent_Kinetic_Energy = 1.0e-6

      End  Inflow Boundary Condition On Surface surface_10

      # Inflow
      Begin Inflow Boundary Condition On Surface surface_11
        X_velocity = 0.0
        Y_velocity = 0.0
$        Z_velocity = .323 $ avg from inlet data
        function for Z_velocity = inlet_vel11 IN THE X DIRECTION
        Temperature = 294.15
        Mixture_Fraction = 0.0
        Turbulent_Kinetic_Energy = 1.0e-6

      End  Inflow Boundary Condition On Surface surface_11

      # Inflow
      Begin Inflow Boundary Condition On Surface surface_12
        X_velocity = 0.0
        Y_velocity = 0.0
$        Z_velocity = .323 $ avg from inlet data
        function for Z_velocity = inlet_vel12 IN THE X DIRECTION
        Temperature = 294.15
        Mixture_Fraction = 0.0
        Turbulent_Kinetic_Energy = 1.0e-6

      End  Inflow Boundary Condition On Surface surface_12

      # Inflow
      Begin Inflow Boundary Condition On Surface surface_13
        X_velocity = 0.0
        Y_velocity = 0.0
$        Z_velocity = .323 $ avg from inlet data
```

```
        function for Z_velocity = inlet_vel13 IN THE X DIRECTION
        Temperature = 294.15
        Mixture_Fraction = 0.0
        Turbulent_Kinetic_Energy = 1.0e-6

      End  Inflow Boundary Condition On Surface surface_13

      # Inflow
      Begin Inflow Boundary Condition On Surface surface_14
        X_velocity = 0.0
        Y_velocity = 0.0
$        Z_velocity = .323 $ avg from inlet data
        function for Z_velocity = inlet_vel14 IN THE X DIRECTION
        Temperature = 294.15
        Mixture_Fraction = 0.0
        Turbulent_Kinetic_Energy = 1.0e-6

      End  Inflow Boundary Condition On Surface surface_14

      # Inflow
      Begin Inflow Boundary Condition On Surface surface_15
        X_velocity = 0.0
        Y_velocity = 0.0
$        Z_velocity = .323 $ avg from inlet data
        function for Z_velocity = inlet_vel15 IN THE X DIRECTION
        Temperature = 294.15
        Mixture_Fraction = 0.0
        Turbulent_Kinetic_Energy = 1.0e-6

      End  Inflow Boundary Condition On Surface surface_15

      # Inflow
      Begin Inflow Boundary Condition On Surface surface_16
        X_velocity = 0.0
        Y_velocity = 0.0
$        Z_velocity = .323 $ avg from inlet data
        function for Z_velocity = inlet_vel16 IN THE X DIRECTION
        Temperature = 294.15
        Mixture_Fraction = 0.0
        Turbulent_Kinetic_Energy = 1.0e-6

      End  Inflow Boundary Condition On Surface surface_16

      # Inflow
      Begin Inflow Boundary Condition On Surface surface_17
        X_velocity = 0.0
        Y_velocity = 0.0
$        Z_velocity = .323 $ avg from inlet data
        function for Z_velocity = inlet_vel17 IN THE X DIRECTION
        Temperature = 294.15
        Mixture_Fraction = 0.0
        Turbulent_Kinetic_Energy = 1.0e-6

      End  Inflow Boundary Condition On Surface surface_17

      # Inflow
      Begin Inflow Boundary Condition On Surface surface_18
        X_velocity = 0.0
        Y_velocity = 0.0
$        Z_velocity = .323 $ avg from inlet data
        function for Z_velocity = inlet_vel18 IN THE X DIRECTION
        Temperature = 294.15
        Mixture_Fraction = 0.0
```

```
        Turbulent_Kinetic_Energy = 1.0e-6

      End  Inflow Boundary Condition On Surface surface_18

$$
      # Inflow
      Begin Inflow Boundary Condition On Surface surface_19
        X_velocity = 0.0
        Y_velocity = 0.0
$        Z_velocity = .323 $ avg from inlet data
        function for Z_velocity = inlet_vel19 IN THE X DIRECTION
        Temperature = 294.15
        Mixture_Fraction = 0.0
        Turbulent_Kinetic_Energy = 1.0e-6

      End  Inflow Boundary Condition On Surface surface_19

      # Inflow
      Begin Inflow Boundary Condition On Surface surface_20
        X_velocity = 0.0
        Y_velocity = 0.0
$        Z_velocity = .323 $ avg from inlet data
        function for Z_velocity = inlet_vel20 IN THE X DIRECTION
        Temperature = 294.15
        Mixture_Fraction = 0.0
        Turbulent_Kinetic_Energy = 1.0e-6

      End  Inflow Boundary Condition On Surface surface_20


      # Inflow
      Begin Inflow Boundary Condition On Surface surface_21
        X_velocity = 0.0
        Y_velocity = .044 $ avg injection velocity (given)
        Z_velocity = 0.0
        Temperature = 294.15
        Mixture_Fraction = 1.0
        Turbulent_Kinetic_Energy = 1e-6

      End  Inflow Boundary Condition On Surface surface_21

      # Open
      Begin Open Boundary Condition On Surface surface_23
        Pressure = 0.0
        Temperature = 294.15
        Mixture_Fraction = 0.0
        Turbulent_Kinetic_Energy = 1e-6 $ low TI

      End  Open Boundary Condition On Surface surface_23


      # Wall Surface
      Begin Wall Boundary Condition On Surface surface_22
        Temperature = 294.15
      End  Wall Boundary Condition On Surface surface_22

      # Wall Surface
      Begin Wall Boundary Condition On Surface surface_24
        Temperature = 294.15
      End  Wall Boundary Condition On Surface surface_24


$-----------------------------------------------------
```

```
$      Define parameters for checkpoint/restart file
$-------------------------------------------------------
      Begin Restart Data Restart
        Input Database Name = rsout/waterChannel.rsout
        Output Database Name  = rsout/waterChannel.rsout
        At Time 5 Increment = 5
      End  Restart Data Restart

   BEGIN AVERAGING AVG
    REYNOLDS AVERAGE FIELD X_velocity AS reynolds_x
    REYNOLDS AVERAGE FIELD Y_velocity AS reynolds_y
    REYNOLDS AVERAGE FIELD Z_velocity AS reynolds_z
    REYNOLDS AVERAGE FIELD mixture_fraction AS avg_mix
    STARTING TIME = 5.1
   END AVERAGING AVG


$-------------------------------------------------
$      Define contents of binary plot file
$-------------------------------------------------
      Begin Results Output Label Output
        Database Name = exodus/waterChannel.e
        At Time 0, Increment = 0.05
        Title Flow Around Building Array
        Nodal Variables = X_velocity As U-x
        Nodal Variables = Y_velocity As U-y
        Nodal Variables = Z_velocity As U-z
        Nodal Variables = Pressure As P
        Nodal Variables = Mixture_Fraction As Mix
        Nodal Variables = Turbulent_Kinetic_Energy As Tke
        Nodal Variables = Turbulent_viscosity As Tmu
$        NODAL Variables = gas_volume_fraction AS gasVol
      End  Results Output Label Output

      Begin Results Output Label Output2
        Database Name = exodus/waterChannel2.e
        At Time 20.0, Increment = .05
        Title Flow Around Building Array

        NODAL Variables = reynolds_x As reynolds_x
        NODAL Variables = reynolds_y As reynolds_y
        NODAL Variables = reynolds_z As reynolds_z
        NODAL Variables = avg_mix

     End  Results Output Label Output2


    End  Fuego Region Fuego_region

  End  Fuego Procedure Fuego_procedure

End  Sierra Fuego
```

DISTRIBUTION

1	MS0899	Technical Library	9532 (electronic copy)


Sandia National Laboratories